

# Microcomput

## 24. Microcomputed Tomography

Angela S.P. Lin , Stuart R. Stock, Robert E. Guldberg 

Since Röntgen discovered x-rays at the end of the nineteenth century and established their usefulness for medical diagnostics imaging, many technological advances have allowed for x-rays to be employed in even more powerful ways. This includes utilizing x-rays for tomographic imaging and quantification.

This chapter describes the principles of microcomputed tomography (microCT) and its use in obtaining internal structural and compositional data about materials/objects of interest. The authors introduce this material with a brief history of the development of laboratory and synchrotron microCT for engineering, biology, and biomedical applications.

As will be evident, microCT imaging requires many components to operate together with precision, and the standard microCT subsystems will be described. This chapter will also explain the principles behind x-ray attenuation in materials as well as common methods by which microCT image processing software may handle complex detected data to reconstruct grayscale slice images. The quality of the resulting images relies on a few key factors, including spatial resolution, noise, and contrast, and these concepts will be explained. Additionally, microCT image reconstruction and processing may produce various types of artifacts, and the most common of these artifacts will be discussed.

In a typical microCT imaging workflow, the reconstructed two-dimensional (2-D) slice images can subsequently be processed to generate segmentations and three-dimensional (3-D) renderings of the material(s) of interest. Because image segmentation and quantification of the material's geometry and composition could be performed via many possible procedures, these processes will be generally discussed within this chapter.

Finally, microCT forms the basis for various novel techniques that are rapidly gaining momentum for use in biology, engineering, and biomedical research applications to provide accurate, non-destructive high-resolution images

and quantitative data. Some of these techniques, such as phase contrast CT, dual-energy CT, fluorescence CT, and x-ray scattering tomography, will be introduced and briefly discussed.

24.1	<b>X-Ray CT</b> .....	1206
24.1.1	Significance and Early Development History .....	1206
24.1.2	Principles of MicroCT and X-Ray Contrast .....	1207
24.1.3	Applications of CT Scanners .....	1208
24.2	<b>MicroCT System Components</b> .....	1210
24.2.1	Laboratory MicroCT Hardware Configuration Types .....	1210
24.2.2	Synchrotron Radiation Equipment Overview .....	1212
24.2.3	X-Ray Source, Spectrum, and Filtering .....	1212
24.2.4	Collimation .....	1213
24.2.5	Specimen Stage, Translation, and Rotation .....	1213
24.2.6	Detectors .....	1214
24.3	<b>Data Acquisition and Image Processing</b> .....	1214
24.3.1	Image Reconstruction .....	1214
24.3.2	System Performance and Image Quality Considerations .....	1218
24.4	<b>Quantitative Analyses and Advanced Post-Processing Methods</b> .....	1224
24.4.1	Segmentation .....	1224
24.4.2	Quantitative Capabilities .....	1225
24.4.3	Image Export and Further Analyses .....	1225
24.5	<b>Other Variants and Recent Developments</b> .....	1226
24.5.1	Synchrotron .....	1226
24.5.2	NanoCT .....	1228
24.5.3	In Vivo Imaging .....	1228
24.5.4	Phase Contrast .....	1228
24.5.5	Dual Energy .....	1229
24.5.6	Fluorescence .....	1230
24.5.7	X-Ray Scattering Tomography .....	1230
24.5.8	In Situ/In Operando/Real-Time Tomography .....	1230
24.6	<b>Summary</b> .....	1232
	<b>References</b> .....	1232

## 24.1 X-Ray CT

X-ray computed tomography (CT) nondestructively reconstructs the interior of objects from a series of projections of the x-ray beam through the object, and x-ray microCT is the high-resolution CT variant for small objects. The term tomography derives from the Greek verb *to cut*, and the term *computed* refers to use of a mathematical reconstruction algorithm combining the projections into slices of the object's cross section.

### 24.1.1 Significance and Early Development History

X-ray computed tomography began to replace analog focal plane tomography in the early 1970s [24.1, 2], and high-resolution x-ray computed tomography (i. e., microtomography or microCT) was first reported in

the 1980s [24.3–11]. MicroCT systems were developed in response to the need to nondestructively examine materials at higher resolution than provided by conventional CT imaging. Dr. Lee Feldkamp, for example, developed one of the early laboratory microCT systems by assembling a microfocus cone beam x-ray source, specimen holder and staggers, and an image intensifier at Ford Motor Company's Scientific Research Laboratory (Fig. 24.1a) to nondestructively detect damage in ceramic manufactured automobile parts. His work attracted the attention of investigators at Henry Ford Hospital and the University of Michigan interested in understanding the relationship between the microstructure and biomechanical function of trabecular (i. e., cancellous) bone as a critical step towards elucidating mechanisms of skeletal fragility associated with aging

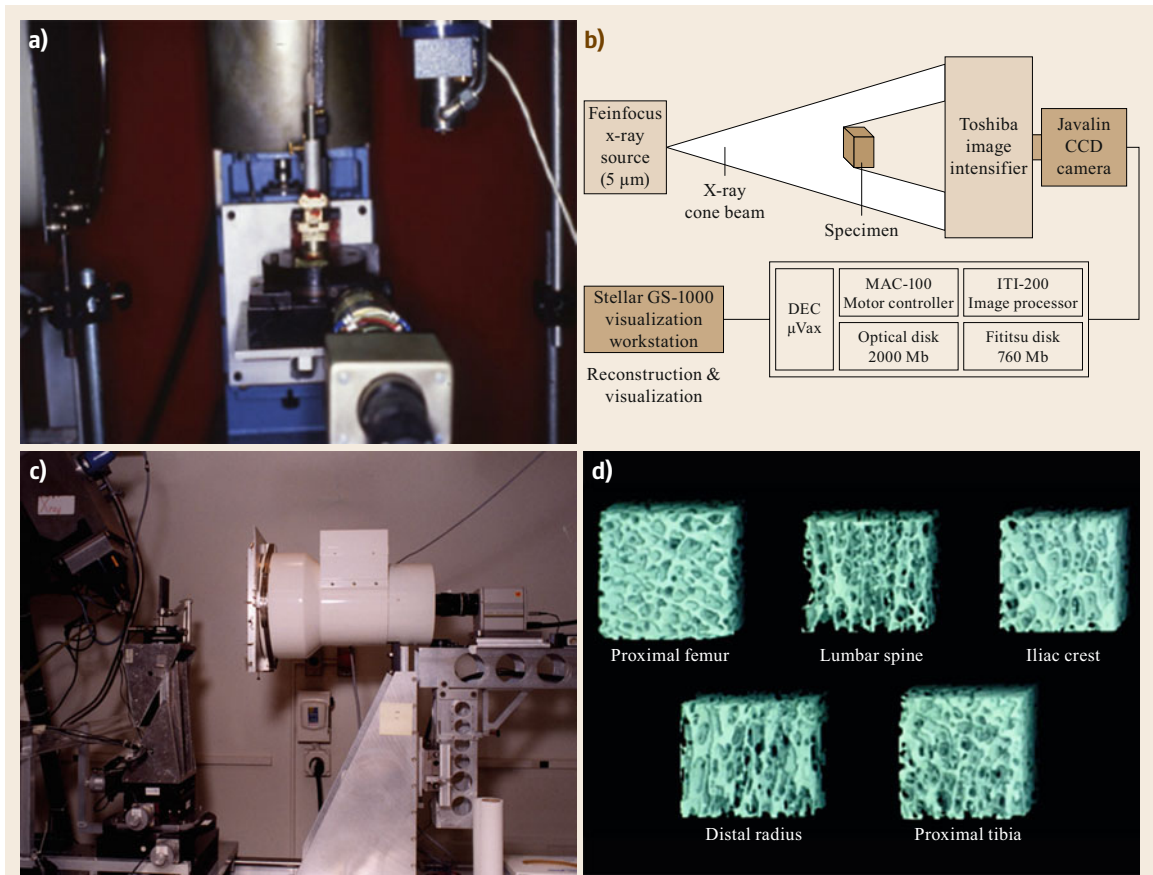


**Fig. 24.1a–d** Early custom-built microCT systems developed by (a) Dr. Lee Feldkamp in Ford Motor Company's Scientific Research Laboratory and (b,c) Professor Steven Goldstein at the University of Michigan with NIH funding. (d) Feldkamp and Goldstein collaborated to examine and quantify the three-dimensional architecture of 8 mm cubes of human trabecular bone from various anatomical sites for the first time

and osteoporotic fractures. The initial proof of concept scans of bone samples were performed at Ford and provided preliminary data for a National Institutes of Health (NIH) grant awarded to Professor Steven Goldstein to construct a microCT system at the University of Michigan and study bone structure-function (Fig. 24.1b–d) [24.6, 9, 10].

Prior to the developments that allowed x-rays to be utilized in tomography, they were widely used in medical diagnostics starting in the early 1900s. X-rays were first discovered in 1895 by Wilhelm Röntgen at the University of Würzburg, Germany, and he won the first Nobel Prize in Physics (1901) for the discovery. Nearly half a century later, short-wavelength synchrotron radiation was first visually observed (1947) at the General Electric Research Laboratory in the United States. Originally seen as a by-product of an investigation into radiation losses in betatrons (magnetic-induction particle accelerators that produce high-energy x-rays), synchrotron radiation was soon determined to have exceptional characteristics that could have an impact in fields like spectroscopy. Interest in the capabilities of synchrotron radiation rapidly grew, leading to the establishment of the first synchrotron facilities in the early 1960s based on older accelerators that had outlived their previous usefulness. In the mid- to late 1960s, the development of electron storage rings, beginning with Tantalus I at the University of Wisconsin, provided improved availability, spectral brightness, radiation flux, stability, and safety for synchrotron radiation work. Second-generation dedicated synchrotron facilities became more widely constructed in the 1970s and early 1980s. The first of these was the Synchrotron Radiation Source (SRS) at the Daresbury Laboratory in the UK [24.12–14]. This was closely followed by construction of the US National Synchrotron Light Source (NSLS) at the Brookhaven National Laboratory and the University of Wisconsin Synchrotron Radiation Center's Aladdin storage ring (replacing Tantalus I), as well as facilities in Japan (Photon Factory, KEK), Germany (BESSY), and France (LURE). Today's third-generation synchrotron facilities use a new generation of storage rings possessing lower emittance and even higher spectral brightness and spatial coherence, and the first of these to be operational was the European Synchrotron Radiation Facility (ESRF) in Grenoble, France.

Modern synchrotron facilities are able to provide microCT imaging capabilities with significant advantages over laboratory microCT systems, such as higher resolution, fewer artifacts, and high contrast sensitivity. The accessibility and overall number of synchrotron facilities in the world continues to grow, making it more feasible for many researchers to overcome previously

prohibitive usage issues such as high costs and scheduling constraints. However, advances in technology and techniques that push toward higher spatial resolution and more efficient scan processes allow today's laboratory microCT systems to provide excellent image quality that in certain applications can compete with synchrotron radiation-based microCT, with certain advantages in ease of use and cost effectiveness [24.15].

### 24.1.2 Principles of MicroCT and X-Ray Contrast

X-ray CT mathematically combines a series of projections into a cross-sectional map of the specimen, and some of the various algorithms for reconstructing images are covered in Sect. 24.3.1. Each projection, regardless of how it is acquired, involves a beam that proceeds from the x-ray source through the sample and onto the detector, and, typically, a single rotation axis and rotation ranges of 180° or 360° are used to record the projections required for reconstruction. Each projection can be broken down into a series of *rays* passing through the sample, and, to a first approximation, each ray is independent of the adjacent rays. The total effect on a given ray is the sum of the effects produced by each successive volume element (voxel) through which it passes, each ray samples a different column of voxels, and the rays in different projections, as dictated by geometry, sample different combinations of voxels.

When x-radiation passes through a specimen, the x-ray beam interacts with the sample in different ways depending on the x-ray energies and the atomic elements encountered. For *low-energy* x-rays, the photoelectric effect and elastic scattering dominate and modify the incident x-ray beam intensity and direction. At much higher x-ray energies, Compton scattering also affects the x-rays passing through the specimen. The beam of x-rays exiting the specimen carries information on the sample, and tomographic reconstruction relies on comparing the incident and exit beams. The focus in this chapter is on x-ray absorption contrast revealed by differences in linear attenuation coefficient  $\mu$ ; this is the most widely used form of microCT. Changes in other signals can be used for reconstruction, including refractive index (phase contrast), crystallographic structure (x-ray diffraction contrast), elemental distribution (fluorescence contrast), particle size and shape (scattering contrast), and local atomic environments (e.g., x-ray absorption near-edge structure, XANES). The modalities other than absorption are discussed in separate subsections below.

In order to understand the contrast within reconstructions with x-ray absorption CT, first consider the x-ray interaction for a single ray passing through a sin-

gle material. For incident x-ray intensity  $I_0$ , the intensity  $I$  of x-rays transmitted through the specimen of thickness  $t$  is

$$I = I_0 e^{-\mu t}, \quad (24.1)$$

where  $\mu$  is the linear attenuation coefficient (units  $\text{cm}^{-1}$ ) which depends on the type and number of atoms traversed by the beam. If  $i$  elements are present, the effective  $\mu$ , denoted  $\langle \mu \rangle$ , depends on the weight fraction  $w_i$ , mass attenuation coefficient  $(\mu/\rho)_i$ , and density  $\rho$  through

$$\langle \mu \rangle = \sum_i w_i \left( \frac{\mu}{\rho} \right)_i \rho. \quad (24.2)$$

Away from absorption edges and in the *moderate* energy range,  $(\mu/\rho) \approx Z^4 \lambda^3$ , where  $Z$  is the atomic number,  $\lambda$  is the x-ray wavelength (inversely proportional to the x-ray energy  $E$ ), and where *moderate* refers to the energy range for a given  $Z$  where photoelectric effect is the main interaction.

Equation (24.1) describes the integrated effect of a uniform sample on the beam passing through it. The task in CT, however, is to determine  $\mu$  with each voxel within the sample. Here for simplicity, consider a single slice within the sample consisting of voxels with

volume  $\Delta V$  and edge length  $\Delta t$  (Fig. 24.2). Each voxel  $j$  along a given path contributes to the total absorption, and these sum to the absorption measured outside the sample

$$\sum_i \mu_i \Delta t = \ln(I_0/I). \quad (24.3)$$

Note that (24.3) is often written in integral form. Figure 24.2 is a schematic of a sample containing three materials of differing absorptivity (darker equals more attenuation) and shows the absorption profiles at  $0^\circ$  and  $90^\circ$  orientations. The voxels along row  $m$  and column  $n$  are shown explicitly. After absorption profiles are collected at enough viewing angles, one of various reconstruction algorithms, described below, combines the absorption profiles at different angles into a map  $\mu(x, y)$  of the slice. The reconstruction problem appears trivial for the sample shown in Fig. 24.2, but is actually much more complex in practice since one typically reconstructs slices with  $10^3 \times 10^3$  or even more voxels.

### 24.1.3 Applications of CT Scanners

Use of CT scanners in medical diagnostics, beginning in the early 1970s, was revolutionary because it vastly improved clinicians' ability to obtain detailed

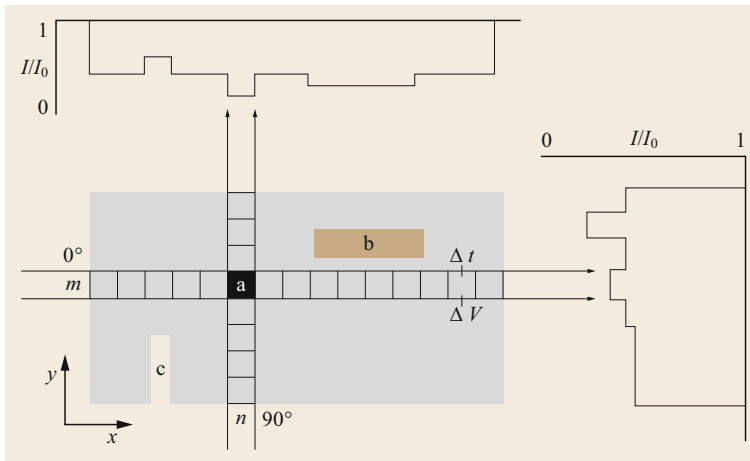


**Fig. 24.2** X-ray absorption profiles for two views through an idealized specimen. Each voxel  $\Delta V$  has edges  $\Delta t$  within the plane and thickness  $\Delta t$  perpendicular to the plane pictured. The ratio  $I/I_0$  is shown schematically for each view and ranges from 1 outside the specimen to a much smaller value depending on the material intercepted. The voxels along the path through row  $m$  and view at  $0^\circ$  orientation are shown as well as those along column  $n$  and  $90^\circ$  orientation. Within the specimen, the darker the gray, the more absorbing the corresponding material. The most highly absorbing material fills a single voxel at  $a$  and produces a narrow decrease in  $I/I_0$  in both views. The four-voxel-long and one-voxel-wide region  $b$  with an intermediate level of absorptivity casts a deep but narrow shadow in the  $0^\circ$  view and a shallow but wide shadow in the  $90^\circ$  view. The crack-like feature at  $c$  is barely visible in the  $0^\circ$  view but, despite being only  $\Delta t/2$  wide, produces a substantial effect on the  $90^\circ$  profile



internal information about human anatomical structures compared to other available noninvasive imaging modalities. CT introduced the capability of acquiring a series of high-resolution virtual sections that could be stacked to form 3-D volumetric data while other techniques only provided 2-D or projection images. These capabilities were extended to nonmedical use in the late 1970s as industrial CT systems were developed for applications involving detection of internal defects in fabricated parts and equipment [24.16, 17].

While industrial CT systems were initially designed with large-scale inorganic materials in mind, improved technologies in the 1980s and 1990s allowed for higher-resolution imaging of small-scale features. The ability to provide nondestructive 3-D imaging at spatial resolution of 100  $\mu\text{m}$  and higher has opened doors to many engineering applications [24.4, 7, 8, 18, 19].

In materials science and mechanics, some of these application areas include microcrack detection and fatigue behavior, characterization and design of porous structures, analysis of composite materials, and

fiber/fabric geometry quantification [24.3, 20–42]. Figure 24.3 provides a few examples of images from microCT scans of inorganic materials and composites.

One of the primary initial applications of laboratory microCT systems was to provide nondestructive imaging capabilities for quantifying the microstructure of organic materials, particularly mineralized bone tissue and the relationships between the mechanical behavior of bone to its structural and compositional properties [24.5, 6, 10, 29, 43–67]. Since the 1990s, microCT techniques have also evolved to include imaging of soft tissues and vasculature using radio-opaque contrast agents [24.68–73]. Figure 24.4 includes examples from microCT imaging of such biological tissues.

An estimated 2500 microCT systems are in use worldwide with currently over 1000 publications annually [24.74]. The use of microCT has grown into a mainstream imaging modality that is regarded as the gold standard for producing quantitative measurements in many application areas, particularly bone morphometry.

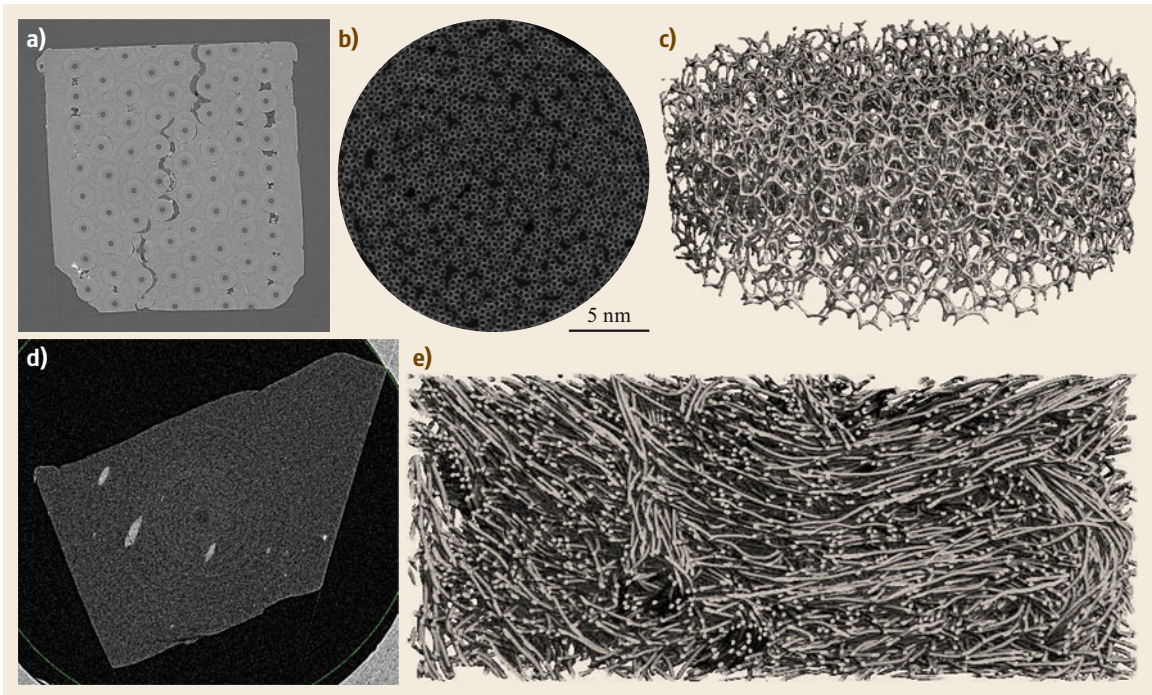


**Fig. 24.3a–e** Reconstructed 2-D grayscale slice images and 3-D binarized renderings of materials examined via microCT; scans performed at voxel sizes ranging from 1–30  $\mu\text{m}$ . **(a)** Silicon carbide (SiC) monofilament-reinforced aluminum matrix, with cracks produced by driving a razor blade into the specimen, parallel to fiber axes. **(b)** 2-D slice tomogram from a cross section of a cylinder composed of sintered nickel tubes. **(c)** 3-D rendering of a porous cellulose foam. **(d)** Slice tomogram of a glass-polymer composite (glass = bright regions). **(e)** 3-D rendering of a nonwoven fabric, virtually sectioned along the longitudinal plane to examine interior fiber orientation

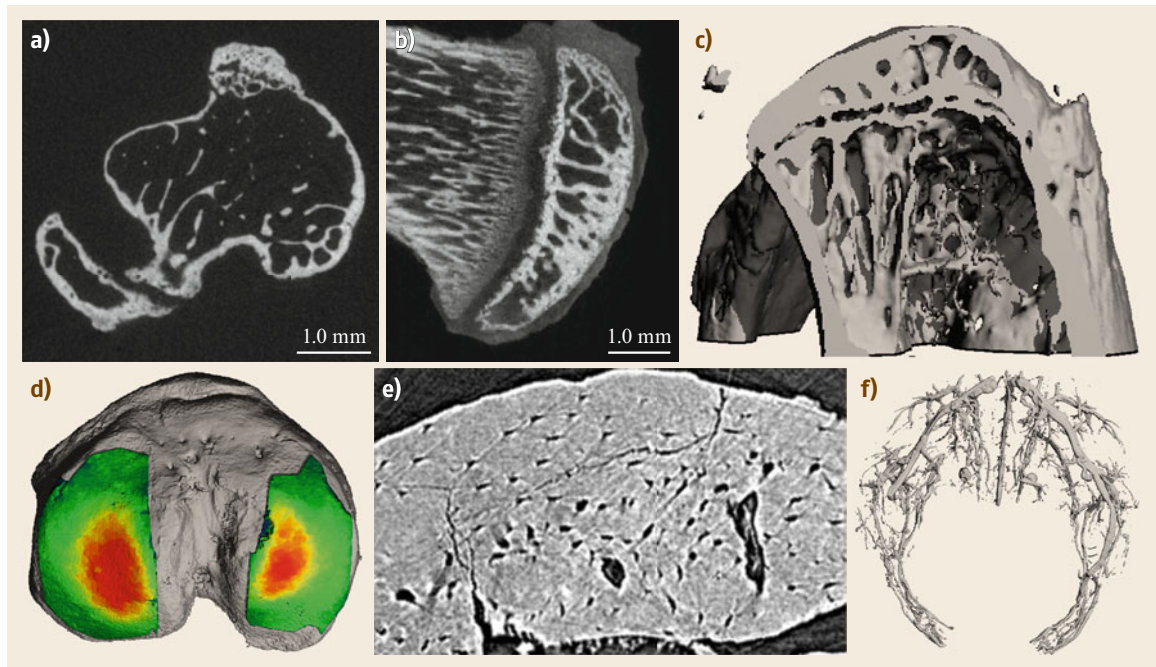


**Fig. 24.4a–f** Images from ex vivo microCT scans of biological tissues; scanned at voxel sizes ranging from 1–30  $\mu\text{m}$ . **(a)** 2-D axial grayscale slice tomogram from the proximal tibia and fibula of a mouse and **(c)** virtually sectioned (sagittal) 3-D binarized rendering of the same specimen, both showing trabecular bone structures within the outer cortical bone of the tibia. **(b)** 2-D grayscale sagittal section of a rat proximal tibia that has undergone contrast-enhanced procedures to allow for quantification of cartilage morphometry and composition in a degenerated joint. This technique allows for generation of **(d)** 3-D pseudocolor cartilage thickness heatmaps overlaid on the bone segmentation; *red* = thicker cartilage regions, *green* = thinner. **(e)** Synchrotron microCT slice tomogram of a cracked mouse femur. **(f)** 3-D binarized rendering of contrast agent-perfused vascular network of mouse hind limbs

## 24.2 MicroCT System Components

Components of laboratory and synchrotron-based microCT systems will be discussed in this section.

### 24.2.1 Laboratory MicroCT Hardware Configuration Types

The history of laboratory microCT has included the development of four scanner hardware configurations: pencil, fan, parallel, and cone beam geometries. All laboratory microCT systems include an x-ray source, a stage or holder space for the object being imaged, and a camera or detector. The four device geometries are differentiated mainly by the type of x-ray source and the type of detector utilized, and two of the geometries utilize beam collimation to narrow and direct the beam prior to reaching the object [24.35].

System components can be extremely simple or quite complex, and variations and details are described

in the subsequent scanner geometry descriptions. Furthermore, system geometries can be categorized into one of four instrumentation generations, but this is largely a legacy from early medical CT devices. Because the laboratory scanner generation nomenclature is still widely used in literature, it will be referenced in this section in the context of describing system geometries and components [24.17, 35, 75].

#### Pencil Beam

Pencil beam systems (Fig. 24.5a) utilize a point-like source and a pinhole collimator to provide a narrow x-ray beam. The specimen is imaged through views that are produced by translation; this allows the beam to cover the entire planar cross section. Successive views or projections are generated through rotation of the specimen, with a full pass constituting a 180° rotation. Signal is collected by a zero-dimensional or point

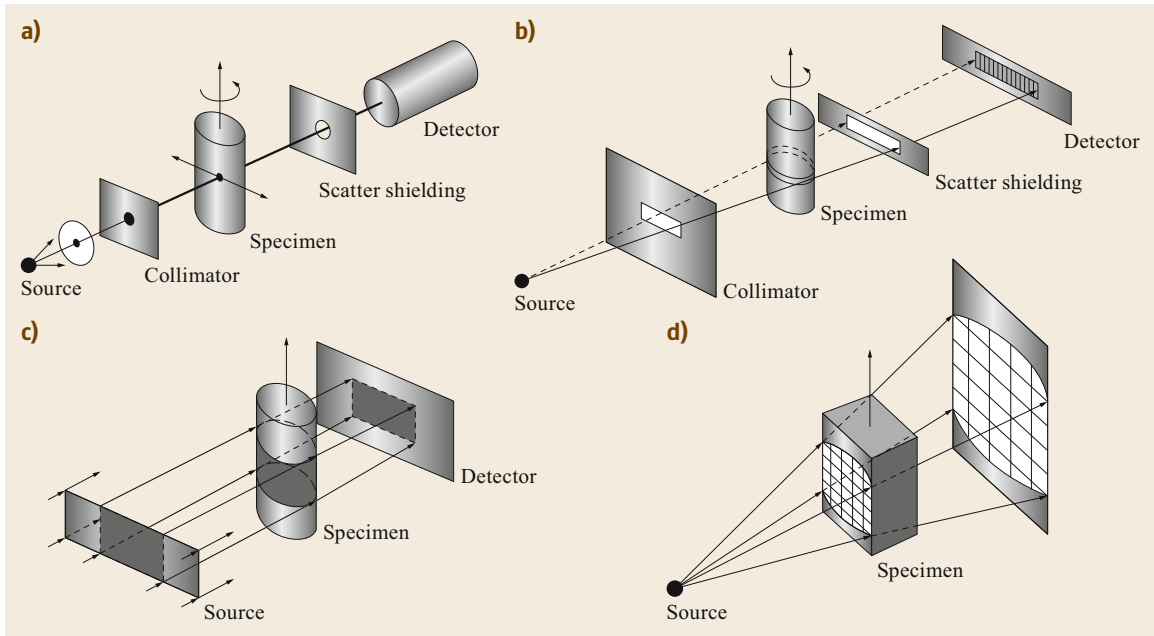


**Fig. 24.5a-d** Illustrations of laboratory microCT scanner geometries: (a) Pencil beam. (b) Fan beam. (c) Parallel beam. (d) Cone beam. Reprinted from [24.35], copyright © The Institute of Materials, Minerals and Mining by permission of the publisher (Taylor & Francis Ltd, <http://www.tandfonline.com>) on behalf of The Institute of Materials, Minerals and Mining

detector, with the possibility of using scatter shielding prior to reaching the detector. The advantages of this system type are that the components are fairly simple, and very accurate linear attenuation values rivaling those obtained with monochromatic radiation are achievable. The disadvantages are that obtaining volumetric data, or images of many sequential slices, is not feasible because scan times would be too long. Scanners employing this hardware geometry are also known as first-generation systems.

#### Fan Beam

In the fan beam geometry (Fig. 24.5b), a point-like source is utilized, much like in the pencil beam geometry. However, the collimator in this design produces a flat fan of x-rays that cover the transaxial dimension of the object. Scatter shielding can be used prior to the signal reaching the detector. The simplest iteration of this type of system uses a detector consisting of a one-dimensional linear array of elements, allowing one entire view or projection to be captured at once. Successive projections are generated through rotation. While this design allows for much more data to be collected at a faster rate than a pencil beam scanner, only data from one slice are captured in each full 180° rotational pass. Two-dimensional area detectors were eventually incorporated to allow for collection of data for more than one slice at a time. The advent of this

type of scanner allowed volumetric data collection to be much more feasible. However, the increased complexity of signal received by the detector array as well as increased effects of scatter resulted in the need to address certain issues such as ring artifacts and other reconstruction challenges. The fan beam geometry is used in second-, third-, and fourth-generation microCT scanners, with varying configurations of source and detector motion relative to the specimen.

#### Parallel Beam

In a fan beam geometry, the beam at any given projection angle diverges from the center (shaped like a fan), whereas in a parallel beam system, x-rays at each projection angle are parallel to one another (shaped like a rectangle, Fig. 24.5c). This requires a spatially wide source (which could be accomplished through collimating optics) as well as a two-dimensional area detector array. The ability to provide parallel beams of x-rays combined with more advanced detector arrays further advanced the speed at which volumetric data could be obtained.

#### Cone Beam

The cone beam geometry utilizes an x-ray beam that at any given projection angle diverges from the center in both the transaxial and axial directions (shaped like a cone, Fig. 24.5d). This results in the ability to cap-



ture data from a greater height of the object in each rotational pass, but also the disadvantage of possible increased image artifacts from the more divergent angle x-rays at the cone beam edges. On the two-dimensional detector array, each detector line or row receives contributions from more than one slice of the object, requiring sophisticated cone beam reconstruction algorithms that will be described in later sections of this chapter. These systems are extremely well suited for rapid collection of 3-D volumetric images and data, and many versions of this microCT scanner geometry are commercially produced and in current use for biomedical and materials research.

### 24.2.2 Synchrotron Radiation Equipment Overview

Synchrotron radiation is produced as charged particles are accelerated at high speeds in a curved path or orbit. Synchrotron radiation facilities that produce x-rays for imaging experiments use large storage rings to accelerate and store electrons and high-field insertion devices to provide shorter-wavelength radiation. Figure 24.6 contains a schematic of a synchrotron facility.

Facilities that allow users to apply for imaging time typically contain many separate beamlines customized for different types of research. Beamlines are physical experimental spaces containing sets of equipment for bringing the x-ray beam to the object. A beamline consists of an aligned set of compartments, each performing specific tasks. One compartment is typically called the optics cabin and modifies the raw x-ray beam using specialized mirrors or optics. Typically, monochromatic radiation is delivered by the optics. Another compartment is commonly called the experimental cabin and has sample holders, movement equipment (amongst other specialized systems to dictate the specimen environment), and detectors. The third is known as the control cabin and contains custom devices and software for controlling the sample, x-ray beam, and data collection tools.

### 24.2.3 X-Ray Source, Spectrum, and Filtering

All laboratory microCT systems contain a source for ionizing radiation, specifically x-rays, and in typical modern laboratory scanners, this comes in the form of a microfocus tube of relatively small size that provides

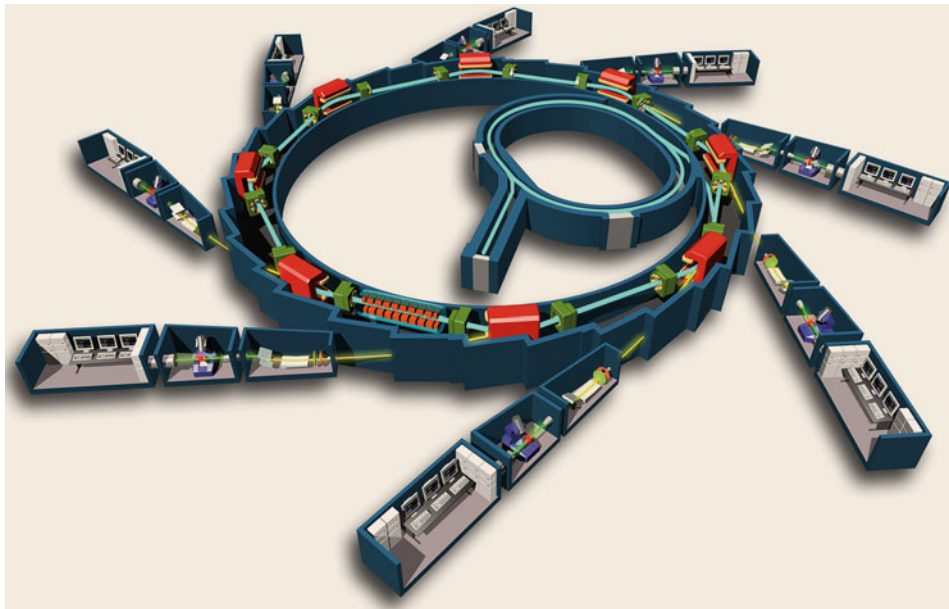


**Fig. 24.6** Schematic of Synchrotron SOLEIL, in Saint-Aubin, France. The outer circular ring is the synchrotron, i. e., a particle accelerator that brings electrons to very high speeds, shown as the light blue beam. The electrons are accelerated by electric fields in the straight sections between *green squares*. The *red rectangles* are magnets that bend the beam. When the beam is bent, electrons emit synchrotron radiation (*yellow*). Beamlines are shown as the lines branching out of the synchrotron. Each beamline contains scientific instruments that focus the beam, hold, and control the specimen, and take measurements [24.76]. Reprinted from EPSIM 3D/JF Santarelli, Synchrotron Soleil. Copyright © EPSIM 3D/JF Santarelli, Synchrotron Soleil. Date 18 Oct 2005



polychromatic radiation, or radiation in a range of wavelengths. Within the tube source, electrons flow through a filament at the cathode end at a specified potential and are accelerated toward the anode end, which contains a metallic target (Fig. 24.7). As electrons strike the target, they decelerate as well as transition between shells, producing bremsstrahlung (or continuous spectrum of x-rays) and characteristic radiation (sharp peaks at certain energies, dependent on the target material). Only a limited amount of the original energy is converted to x-ray energy. Additionally, x-rays emerge from the target in all directions, limiting the amount of x-rays that will actually be emitted toward the specimen.

The sources used in commercially available laboratory microCT systems typically allow the user some degree of flexibility to adjust the maximum energy (or peak voltage, kVp) and tube current ( $\mu\text{A}$ ) for each scan in order to produce different imaging conditions. Increasing energy allows more penetration of the material such that higher absorbing materials may be imaged more easily. Decreasing voltage and increasing current may facilitate better detection of contrast differences between lower absorbing materials.

In contrast to the compact nature of typical laboratory microCT x-ray sources, synchrotron facilities

generate x-rays in a large circular particle accelerator known as a storage ring that may have a circumference of many miles. Using a controlled assembly of magnets to steer the particles and high vacuum conditions to minimize loss of particles due to deflection, electrons are accelerated in a circular path to maintain their energy (Fig. 24.6, *light blue* beam path). The radiation is then projected at tangents from the storage ring and captured in beamlines, or spaces designed to provide x-ray beam characteristics (spectrum, energy, dimensions, flux, etc.) for specific experimental applications.

Resulting beam characteristics for each beamline can be controlled in many ways prior to reaching a compartment where it will come in contact with the specimen. Beamlines originating from one of the storage ring bending magnets will have different spectrum and energy than those originating from one of the straight sections of the storage ring. The beamline's optical cabin will also contain devices (e. g., slits, attenuators, monochromators, and mirrors) that will define its bandwidth, flux, beam dimensions, focus, and collimation. An illustration of the SOLEIL Synchrotron in Saint-Aubin, France, is shown in Fig. 24.6 [24.76, 78].

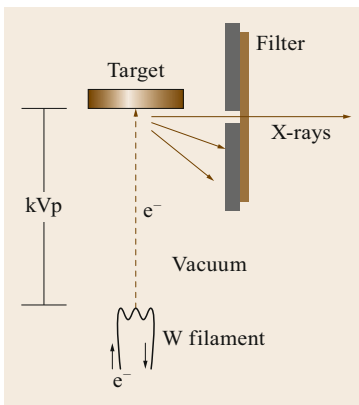


**Fig. 24.7** X-ray tube source illustration. Electrons  $e^-$  flow through a cathode filament (tungsten) and are thermionically accelerated, through a high-vacuum environment such that electrons do not strike air molecules and lose energy, toward an anode target (also tungsten). As electrons strike the target, they decelerate and produce radiation. X-rays comprise only a small fraction of the energy from the beam and are emitted in all directions. As diagrammed in this figure, x-rays then pass through an aperture and filter on their way toward the object. Reprinted from [24.77], copyright © 2008 from Microcomputed tomography: Methodology and Applications by S.R. Stock. Reproduced by permission of Taylor and Francis Group, LLC, a division of Informa plc

#### 24.2.4 Collimation

A collimator is the component of a microCT system that narrows the x-ray beam. Collimation may be needed to shape the emitted x-ray beam or align it such that x-rays remain parallel to a specified direction as the beam travels toward the object. Certain experimental configurations also use scatter slits, a form of collimation to improve image quality.

#### 24.2.5 Specimen Stage, Translation, and Rotation

The mechanical motions required in most microCT systems include positioning the object at the appropriate distance from the source, rotating the object about the central axis of the field of view, translating the object vertically to reach subsequent slices or stacks, or rotating the source and/or detector about the object. These actions must be performed accurately and precisely (much smaller than the system's smallest possible reconstruction voxel size) as well as with stability across the passage of time to ensure reproducibly good image quality [24.79]. Additionally, the holder that contains the specimen must be fabricated such that the possibility of relative shifting or wobbling with respect to the specified imaging motions is minimized. Thus, high-quality mechanical components such as precision mechanical bearings or air bearings and tightly toleranced fabrication processes must be utilized. Com-

pensatory algorithms can sometimes be used to adjust for imperfections in mechanical motion control, but reliance on these should be avoided.

### 24.2.6 Detectors

MicroCT detector arrays are based on semiconductor devices that are excellent for detecting visible light. These are coupled to an x-ray scintillator to reduce the device's susceptibility to radiation damage. The scintillator consists of a thin phosphor film (granular or single crystalline), and x-rays are absorbed in this layer and emit optical wavelengths which an array of lenses or fiber-optics bring to the detector elements [24.79].

Most modern microCT systems use two-dimensional charge-coupled devices (CCDs) in their detector arrays. The individual elements or pixels are capacitors that, during the initial exposure or image integration

phase, first passively collect optical photons and convert them proportionally to electron charges. These elements have a specific maximum capacity for collection, called the well depth [24.80], which is typically  $10^5$  electrons [24.80, 81]. After the exposure phase comes the readout phase. Here, the electron charge levels in each pixel are read out and converted to digital values through a series of charge shifts from one pixel to the next across the entire area of the CCD until each value is recorded. During the readout phase, the detector elements cannot be used to collect photons. Larger detector elements can store greater numbers of electrons, producing a greater dynamic range [24.79]. However, storing a greater number of electrons also increases the time required for the readout phase. Faster readout is necessary to expedite this phase, but this can result in errors in the elemental charge measurements, which can lead to higher overall noise levels [24.80].

## 24.3 Data Acquisition and Image Processing

### 24.3.1 Image Reconstruction

As described in Sect. 24.1.2, projections along different viewing directions provide the data necessary for reconstructing specimens. For simplicity, the descriptions in Sect. 24.3.1, *Iterative Approaches*, and Sect. 24.3.1, *Back Projection and Transform Methods*, assume that the projection data for reconstructing each cross section or slice is independent of that for the adjacent slices; as is illustrated above, this is not true for cone beam or spiral CT which require additional numerical processing before reconstruction. It is important to remember that each reconstructed slice is an array of voxels with non-zero thickness normal to the slice plane: each slice is a thin, flat slab and not a plane.

The reconstruction algorithms in widespread use can be classified into two types: iterative methods (Sect. 24.3.1, *Iterative Approaches*) and transform methods (Sect. 24.3.1, *Back Projection and Transform Methods*). Each class of methods offers different strengths and weaknesses, and, within each, there are a variety of approaches which cannot all be covered here. *Kak and Slaney* [24.18] provide much more detailed yet accessible coverage.

#### Iterative Approaches

Equation (24.3) expresses how each voxel along a given path or ray contributes to produce the total decrease in x-ray intensity  $\ln(I_0/I)$ ; in terms of the schematic in Fig. 24.2, the  $n$  voxels along path  $m$  contribute a content-dependent increment of attenuation. Each of

the  $M$  rows (i. e.,  $M$  rays) in  $0^\circ$  projection direction consists of a similar summation as does each of the  $N$  columns in the  $90^\circ$  orientation, and the same is true over the other viewing directions. This discrete formulation of the specimen's absorption can be represented as a system of linear equations. For row  $m$  of Fig. 24.2, there are 15 terms in the linear equation, and for column  $n$  there are 8 terms in that second equation. For practical samples (e. g., 2048 voxels or more in diameter), the number of terms in each ray's equation is very large; the number of rays for one view is also very large as is the number of views required for accurate reconstruction. In mathematical terms, the rank of the linear equation system is enormous, and it is impractical to solve this system of equations directly.

Iterative methods offer a practical approach to assigning accurate values  $\mu(x, y)$  to the volume scanned, i. e., to determining the internal structure of the specimen. In the iterative approach, the reconstruction space (the volume covered by the projections and containing the specimen) begins as a *blank slate*  $\mu'(x, y)$  to which voxel values must be assigned. Each projected ray sums the absorption of the many voxels intercepted by the ray on its path through the specimen, and the same is true of the other rays forming the radiograph or view. Further, each voxel  $x, y$  within the reconstruction space contributes to only one ray within a view (ignoring any voxels that are split between adjacent rays), and this simple geometry dictates how the set of all voxels contribute to produce a view and how different  $x, y$  combine in different rays in the

various views. When the sample rotates and the next view (radiograph) is produced, the combination of voxels contributing to each ray changes. Reconstruction proceeds by iteratively changing  $\mu'(x, y)$ , i. e., the absorption assigned to each voxel, until the hypothetical set of radiographs derived from  $\mu'(x, y)$  values matches the actual set of radiographs and, ideally,  $\mu'(x, y)$  should match  $\mu(x, y)$ .

In order for  $\mu'(x, y)$  to converge to  $\mu(x, y)$  in a reasonable amount of time, the voxel values must be changed in an organized and efficient process. The approaches described here compute the difference, for each ray of the view, between the experimental radiograph or projection  $\ln(I_0/I)$  and that produced by the hypothetical  $\mu'(x, y)$ , i. e.,  $\ln(I_0/I')$ . The mean difference between experimental and hypothetical values is converted to a constant increment  $\Delta\mu'$  added to (or subtracted from) the values of the voxels lying along the ray under consideration. Numerically, for each ray,

$$\frac{\ln(I_0/I) + \ln(I_0/I')}{2} = \frac{\mu t - \sum_i \mu'_i \Delta t}{2} = \Delta\mu' \quad (24.4)$$

and the new values along this ray are  $\mu'_i + \Delta\mu'$ . In the algebraic reconstruction technique (ART),  $\Delta\mu'$  is computed for a view, and  $\mu'(x, y)$  is updated before the next view is considered. Simplified illustrations of ART appear elsewhere, e. g., Sect. 3.2 of *Stock* [24.77]. The simultaneous iterative reconstruction technique (SIRT) differs from ART in that the value of  $\Delta\mu'$  is not determined on a view-by-view basis. Instead, the value of  $\Delta\mu'$  for each voxel  $x, y$  is calculated by averaging  $\Delta\mu'$  for the voxel from the different views. With all voxels updated, the new  $\ln(I_0/I')$  is compared with  $\ln(I_0/I)$  for the next iteration.

An advantage of iterative approaches over back-projection techniques (see next section) is that it is relatively easy to incorporate prior information into the reconstruction process. Further, with iterative techniques, truncated data (missing views in the set of projections or portions of the cross section moving out of view) or significant angular undersampling may not significantly damage the quality of the reconstruction. A disadvantage of iterative approaches is that reconstruction is much more computationally demanding than for the methods described in the following subsection.

### Back Projection and Transform Methods

Reconstruction via the methods described in this section can take place in one of two virtual spaces, virtual being used to differentiate the spaces from the  $x$ - $y$ - $z$  Cartesian space containing the specimen. First, recon-

struction can be performed in a virtual  $x'$ - $y'$ - $z'$  Cartesian coordinate system, i. e., in what is termed direct space. Second, the direct space data from the projections can be represented in frequency space, i. e., the plane in frequency space can be populated by frequency data projection by projection, and the reconstruction performed by converting the populated frequency space into the slice in direct space.

In back projection, the observed radiographic *absorptivity* is projected back along the direction in which it was obtained, and the absorptivity of each successive view is added to the previously back-projected absorptivity. In simple terms, as more views contribute to the virtual space, absorptivity *builds up* at positions of high absorption in the actual specimen and drops below its surroundings at places where absorptivity is low.

The schematic projections derived from the sample in Fig. 24.2 illustrate reconstruction via back projection (Fig. 24.8). The 90° view is back-projected in Fig. 24.8a, and the 0° radiograph in Fig. 24.8b. The addition of the two views appears in Fig. 24.8c, and it is clear that more information is required to obtain an accurate reconstruction. For example, the very high attenuation voxel a (Fig. 24.2) might be at a or a' in Fig. 24.8c, or two highly absorbing particles might be present. Streaks are present in the reconstruction, particularly along the major axes of features such as b, and such high aspect features can confound detection of high-absorption features such as a when they are aligned within a view. Each of the line of voxels in the crack-like feature c consists of some empty space and some matrix; these partial voxels produce lower contrast and c as pictured is not very visible even when viewed along its plane. Even with partial voxels, c should be much more visible than shown in Fig. 24.8a,c (an artifact of the gray scale employed). Section. 24.3.1, *Sampling Requirements*, discusses the relationship between the number of additional views and fidelity of the reconstruction.

The problems with features a–c in Fig. 24.8c can be resolved with more views. The back projection shows extra mass outside the actual sample and this would not disappear with additional views. Features like a would have a similar halo around them; this is also an artifact. Suppressing these predictable artifacts can be done either in the direct virtual space or in frequency space; the mathematics of accomplishing this follow.

Equation (24.1) reveals what is observed after attenuation is complete, and the contribution of each voxel to the total attenuation is written in discrete form in (24.3). An alternative formulation is to use an integral equation to describe absorption. Each voxel with attenuation coefficient  $\mu_i$  along path  $s$  contributes to the total absorption, and the transmitted intensity can be written

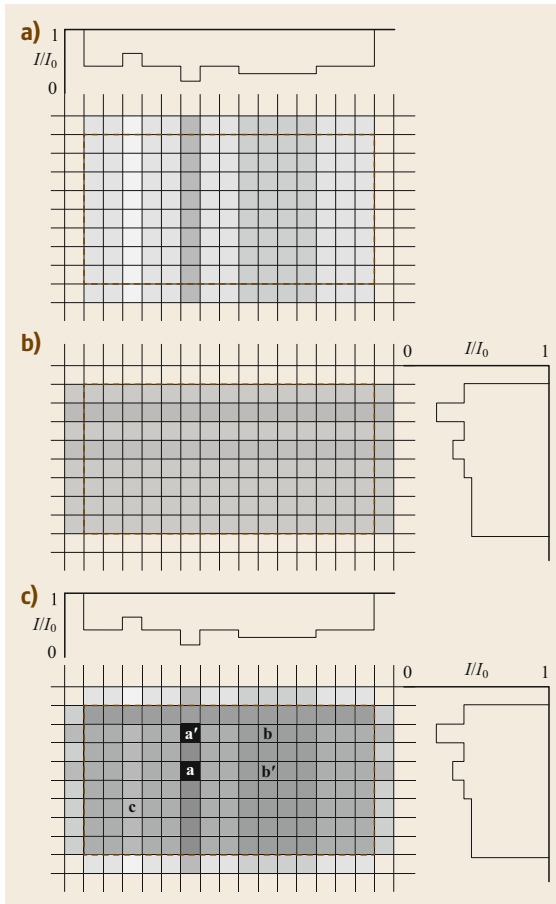


**Fig. 24.8a–c** Simple back projection of the two absorption profiles (i. e., views or radiographs) derived from the specimen in Fig. 24.2. **(a)** 90° back projection of the profile shown in the top of the panel. The dashed line indicates the perimeter of the specimen. **(b)** 0° back projection of the profile shown in the right of the panel. **(c)** Combination of the two back projections. Features (a–c) correspond to those in Fig. 24.2, and a' and b' are not actually present in the specimen. Ten levels of gray are used in the schematic to illustrate the levels of contrast in the back projection

as

$$I = I_0 e^{-\int \mu(s) ds} \tag{24.5}$$

where  $\mu(s)$  is the linear absorption coefficient at position  $s$  along ray  $s$ . Rewriting (24.5) yields

$$\int \mu(s) ds = \ln(I_0/I) = P_s(s) \tag{24.6}$$

i. e., the input for reconstruction are the values of the line integral for the various orientations of  $s$  (projection angle) at all positions across the specimen and for

the set of all  $s$  (projection angles). One needs to combine the views  $P_s(s)$  over all  $s$  to obtain  $\mu(x, y)$ , the reconstructed slice (see [24.75, 77] for more details). Equation (24.6) is rewritten in terms of rotation angle  $\theta$  and position  $\rho$

$$P(\theta, \rho) = \ln[I_0/I(\theta, \rho)] = \int \mu(x, y) ds. \tag{24.7}$$

In the convolution back projection approach, solving for  $\mu(x, y)$  is combined with correcting the halos introduced by back projection. To do this, the function  $P(\theta, \rho)$  is convoluted with a function  $g(r)$  describing the mathematical form of the halos, where

$$g(r) = \left(\frac{\pi^2}{2}\right) \left(\frac{\delta(r)}{r} - r^2\right) \tag{24.8}$$

and  $\delta(r)$  = the Dirac delta function. Incorporating  $g(r)$  and solving for  $\mu(x, y)$  utilizing projection from 0 to 180° (rotations in radians from 0 to  $\pi$ ) yields

$$\mu(x, y) = \iint P(\theta, \rho) g(\rho - \eta) d\eta d\theta, \tag{24.9}$$

where the limits of the first integral are 0 and  $\pi$  and of the second integral are  $-\infty$  and  $\infty$ . Note that (24.8) is not the only filter function that can be used.

In filtered back projection, the observed radiographic absorptivity  $P_s(s)$  is projected back along direction  $s$  into the virtual space representing the reconstructed sample.

Frequency space approaches consider the reconstruction problem in a different fashion. In many applications it can be more informative or more efficient to consider a given problem in frequency space instead of in direct space. In x-ray or electron diffraction, for example, reciprocal space representations (a version of frequency space) are often more instructive than the corresponding direct space data of the single crystal or polycrystalline specimens [24.82].

Figure 24.9 indicates how Fourier transforms of absorption profiles  $P_q$  (in the spatial domain) populate the frequency domain projection by projection. The Fourier components (frequencies and amplitudes along line  $t$ , projected along  $s$  in the spatial domain) of  $P_q$  provide points along line B–B' in the frequency domain. Each frequency is plotted at radius  $r$  along the line shown in Fig. 24.9a, and that frequency's amplitude is the point's numerical value. Data from projections at different angles  $q$  from 0 to 180° fill frequency space (Fig. 24.9b). Because the frequency space representation is as valid as the direct space version of the object (provided, of course, that it is adequately populated with observations), Fourier transformation of the frequency data will



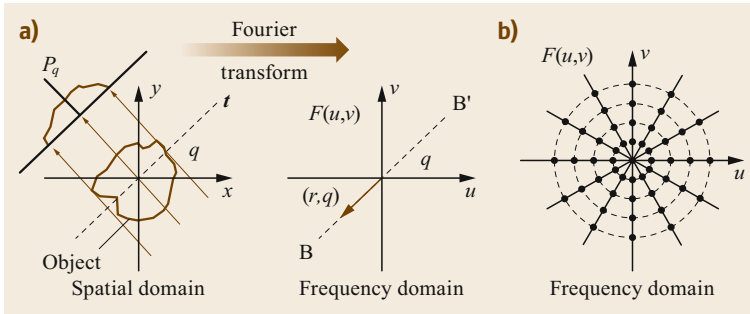


**Fig. 24.9a,b** Relationship between absorption profile in direct and frequency spaces. **(a)** The absorption profile  $P_q$  (along direction  $q$  in the spatial domain, left side of the panel) is treated as a waveform with Fourier components (frequencies and amplitudes along line  $t$ , projected along  $s$  in the spatial domain). The components of  $P_q$  (via Fourier transformation) provide points along line  $B-B'$  in the frequency domain (right side of the panel): Each frequency is plotted at radius  $r$  along  $B-B'$ , and that frequency's amplitude is the point's numerical value. **(b)** Data from projections at different angles  $q$  from  $0$  to  $180^\circ$  fill frequency space. Reprinted from [24.77] Copyright © 2008 from Microcomputed tomography: Methodology and Applications by S.R. Stock. Reproduced by permission of Taylor and Francis Group, LLC, a division of Informa plc

produce a valid reconstruction the object in the spatial domain.

Mathematically, the two-dimensional Fourier transform  $F(u, v)$  of an object function  $f(x, y)$  is

$$F(u, v) = \iint f(x, y) e^{-2\pi i(ux+vy)} dx dy, \quad (24.10)$$

where the limits of integration are  $\pm\infty$ . A projection  $P_q(t)$  and its transform  $S_q(w)$  are related by a similar equation, and, for parallel projections, some mathematical manipulation yields the relationship

$$F(u, 0) = S_{q=0}(u) \quad (24.11)$$

a result independent of orientation between the object and coordinate system. This is a form of the Fourier slice theorem which can be stated as:

#### Theorem 24.1 Fourier Slice Theorem

The Fourier transform of a parallel projection of an image  $f(x, y)$  taken at an angle  $q$  gives a slice of a two-dimensional transform  $F(u, v)$  subtending an angle  $q$  with the  $u$ -axis. In other words, the Fourier transform of  $P_q(t)$  gives values of  $F(u, v)$  along line  $B-B'$  in Fig. 24.9a [24.18].

Collecting projections at many angles fills the frequency domain as shown in Fig. 24.9b, and the inverse Fourier transform

$$f(x, y) = \iint F(u, v) e^{2\pi i(ux+vy)} du dv \quad (24.12)$$

integration limits again at  $\pm\infty$ , can be used to recover the object function  $f(x, y)$ , i. e.,  $\mu(x, y)$ . Often, the fast Fourier transform algorithm is used for these

operations, and interpolation between the spokes of data in the frequency domain is required. Inspection of Fig. 24.9b shows sparser coverage farther from the origin of the frequency space; therefore, the high-frequency components are more subject to error than the lower spatial frequencies.

#### Sampling Requirements

The quality of a reconstruction of an  $M \times M$  object (i. e., a planar slice of  $M$  voxels in one direction and  $M$  voxels along a second direction perpendicular to the first) depends on several factors. These include:

1. How finely the object is sampled, i. e., the spatial frequencies resolved in the profiles  $P(s)$  and the number of viewing directions.
2. How accurately individual measurements of  $\ln(I_0/I)$  are made, i. e., the levels of random and systematic counting errors.
3. How precisely each measurement can be related to a common frame of reference.

The last consideration is the subject of other sections in this chapter. The number of samples per projection and the number of views needed depends on the reconstruction method and on the size of features one wishes to resolve in the reconstruction. The Nyquist sampling theorem [24.18] relates the pixel size in each projection, the number of projections angles recorded, and the smallest dimension (in the slice plane) of reconstructed voxels that contain physical information. For an  $M \times M$  slice, a minimum of  $(\pi/4)M^2$  independent measurements are required if the data are noise-free, but faithful reconstruction can still be obtained

with lower levels of sampling, even in the presence of noise [24.18]. A useful rule-of-thumb is that the number of projections should roughly equal the number of voxels across the region being reconstructed (i.e., the specimen and the empty space surrounding it), but, if other considerations limit data collection, the number of samples per view is generally more important than the number of views. In parallel beam reconstructions with synchrotron x-rays, data acquisition typically is done with 2 K (2048) detector elements across the slice (2 K samples per projection) and  $1.5 \times 10^3$  projections.

The precision of linear attenuation coefficients determined in reconstructions depends on its variance through

$$\sigma_0^2 = \text{const} \cdot v (M_{\text{proj}} \langle N_0 \rangle)^{-1}, \quad (24.13)$$

where  $v$  is the spatial sampling frequency,  $M_{\text{proj}}$  is the number of views, and  $\langle N_0 \rangle$  is the mean number of photons transmitted through the center of the specimen [24.18]. Strictly speaking, (24.13) applies only to the center voxel of the specimen, but this equation provides important guidance in terms of how changes in several parameters affect reconstructed data. For example, consider the mean value of the linear attenuation coefficient ( $\mu$ ) for a region encompassing a significant number of voxels. Reconstructions produced from projections recorded for time  $t_0$  (with  $N_0$  counts per voxel) would have a standard deviation of the linear attenuation coefficient  $\sigma'$ , whereas those recorded for time  $4t_0$  ( $4N_0$  counts) would be expected to have standard deviation equal to  $0.5\sigma'$ , if counting statistics were the sole contribution to the variance. Similarly, for the same counting time and x-ray source, if one were to collect data with two sampling dimensions (voxel sizes)  $v'$  and  $v'/2$ , one would expect the standard deviation of the latter measurement to be substantially larger. Other contributions to broadened distributions of linear attenuation coefficients can be substantial and should not be ignored; these include partial volume effects (voxels partly occupied by two very different phases giving rise to an intermediate value of  $\mu$ ).

Errors in  $I/I_0$  of  $10^{-3}$  affect reconstruction accuracy. The incident beam  $I_0$  is never entirely constant, either over time or over position, and CT requires its precise measurement. Views without the specimen in the beam are typically used for normalization, and these white-field views cannot saturate the detector at any point without degrading the normalization's accuracy. All detectors have a finite contrast range (e.g., a 12-bit detector can nominally measure 4096 contrast levels) and hence the range of  $I/I_0$  that can be used as input for

reconstruction. One can increase the dynamic range in a projection by frame averaging, but this discussion is beyond the scope of the chapter.

For  $M$  voxels across the detector's field of view equal to  $W$ , one typically expects to reconstruct with voxels with edges of  $W/M$ . If  $W = 4$  mm and  $M = 2 \times 10^3$  voxels, then the voxel dimensions are  $\approx 2 \mu\text{m}$ . Features down to one-tenth of the volume of a reconstructed voxel can be seen if contrast is high enough [24.22, 23], and metrology algorithms can measure dimensions to about one-tenth of a pixel with a three-sigma confidence level.

All of the *exact* reconstruction algorithms require a full  $180^\circ$  set of views in which all of the specimen cross-section remains within the field of view. Approximate reconstructions can be obtained where views are missing, for example, where opacity and sample size or where sample chambers limit the directions along which useful views may be obtained; degraded reconstruction quality is a typical consequence with orientation-dependent artifacts. Local or region of interest tomography is a second type of truncated data reconstruction and is typically used when the required voxel size cannot be obtained for a specific cross section  $W$  and number of detector elements  $M$ . If, for example, the required voxel size was  $2 \mu\text{m}$ ,  $W = 8$  mm and  $M = 2 \times 10^3$ , then only 4 mm of the sample could be kept in the field of view. The remainder of the sample would rotate into and out of view; the missing mass affects contrast, but, in most cases, not the geometric fidelity of the reconstruction of high-contrast features. One can avoid local tomography by stitching projections to cover different parts of the specimens and using these enlarged radiographs for reconstruction, but the local tomography approach is often good enough for many applications. Another approximate data collection approach is spiral tomography, discussed in an earlier section, which has received considerable attention because it affords increased speed and lower x-ray dose.

### 24.3.2 System Performance and Image Quality Considerations

The performance of a microCT system can be defined as an assessment of the sensitivity to detect the features of interest in the specific application. However, this question of how well the resulting image data match the actual object encompasses a complex set of concepts regarding image quality, probability of detection, and the perception and skill of the user. In other words, it is possible to create images of extremely high resolution using microCT yet fail to provide appropriate image quality to detect desired features or fail to pro-

vide results that are helpful in the specific application. This section will simplify this discussion by addressing evaluative methods relevant to image quality. There are several factors that can affect image quality, and these must be considered individually as well as in their interactions with one another: spatial resolution, contrast and noise sensitivity, artifacts, and effects of sample preparation [24.16, 17, 75].

### Resolution

MicroCT system specifications often include a range of nominal voxel resolutions, which indicate the range of calculated voxel dimensions based on scanner hardware, particularly detector array type and size. Spatial resolution is more relevant for scanner performance and image quality, as it is a measure of the ability of the system to identify small features and distinguish between two features that are close together [24.16, 17]. System parameters that determine resolution include the size of the x-ray focal spot, size of the detector elements or pixels, scanner geometry, and reconstruction algorithm used. Several methods for characterizing spatial resolution exist.

**Empirical Spatial Resolution Measurement.** Resolution bar phantoms can be used to measure spatial resolution (Fig. 24.10). These blocks of material contain groups of regularly repeating, uniform, high-contrast patterns (usually at a 45° angle to the pixel row pattern of the resulting image) that can be series of parallel slots or parallel bars within the block. Each group of slots/bars has a controlled slot/bar width and slot/bar separation. Spatial resolution is defined as the smallest distance between slots or bars that is distinguishable in the scan image.

**Point Spread Function (PSF).** Another method for characterizing spatial resolution is to measure the point spread function (PSF) of the system, which describes the blurring of an infinitesimally small point-like object [24.16, 75]. The resultant image from any given scan always represents a blurred version of the actual object's density distribution (Fig. 24.11). The PSF allows for characterization of the degree of image blurring or image sharpness. It can be measured by scanning a thin wire (much smaller than the voxel size) positioned perpendicularly to the slice plane. In a perfect system, the image profile would show a sharp transition between background and the wire edges, allowing for a measurement that matches the true width of the wire. In reality, a microCT image will be blurred, which will result in an image profile that is a smoothed and averaged PSF—a bell-shaped curve. This profile's full width at half maximum (FWHM) provides a quantifiable measurement of the sharpness of the image [24.16].

**Modulation Transfer Function (MTF).** The modulation transfer function (MTF) is another measure of resolution and can be mathematically derived from the PSF via normalized Fourier transform [24.16, 75]. Fourier theory states that a signal or object can be described by a series of sinusoidal functions. The MTF is the ratio of the output to input modulation intensities as a function of sinusoidal spatial frequencies (cycles per unit distance). The MTF can also be approximated using resolution bar phantom measurements (Fig. 24.10). Groups of thick bars with low spatial frequency (line pairs per mm) show maximum contrast between the high- and low-density-material lines, resulting in an MTF value of 1.0. For successively thinner

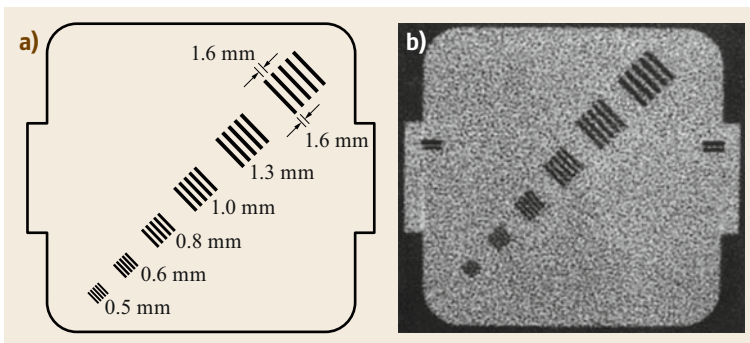


**Fig. 24.10a,b** Spatial resolution can be measured by imaging a bar phantom, which contains groups of parallel bars, typically positioned at a 45° angle to the pixel rows. **(a)** Schematic of bar phantom with six groups of five parallel bars; each group has a defined constant width and separation, as noted on the schematic. The bars are typically filled with water to provide a certain amount of contrast. **(b)** After scanning with microCT, spatial resolution is determined from the defined bar separation in the group with the smallest discernible spacing. From [24.16]. Copyright 1994 by The Minerals, Metals & Materials Society. Used with permission

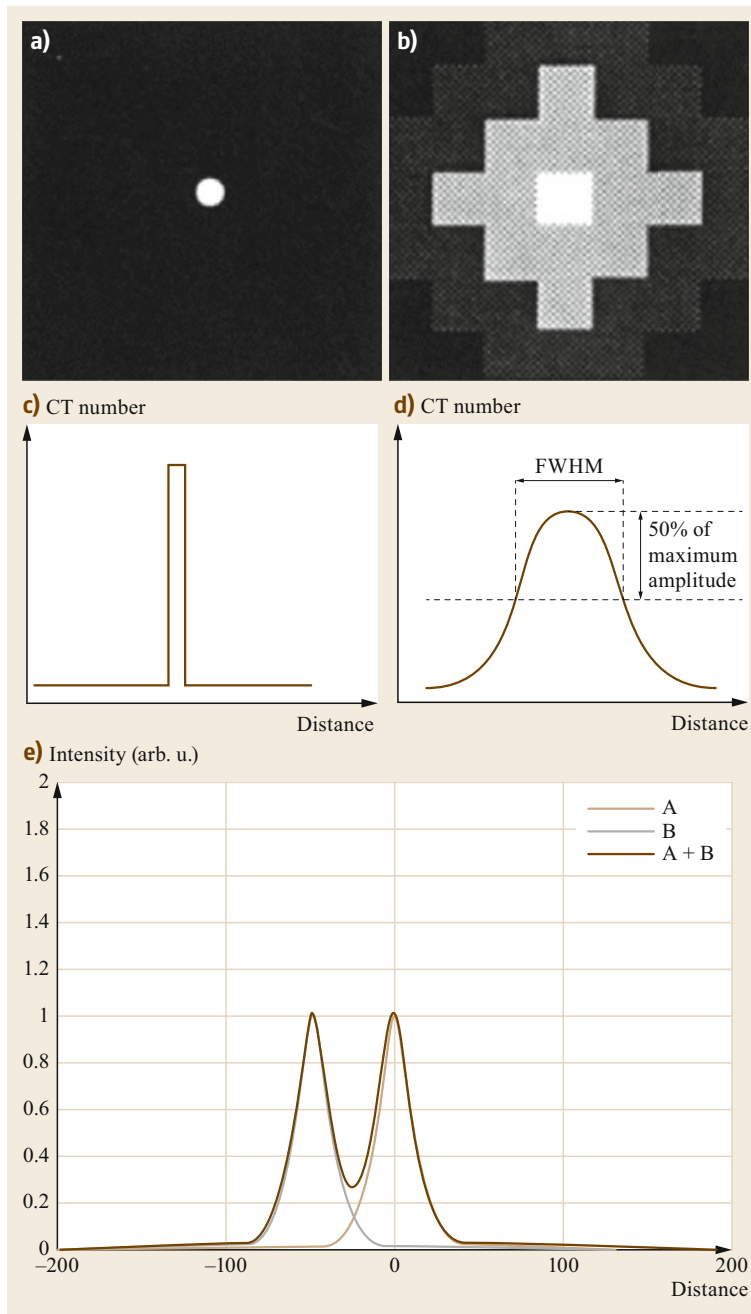


**Fig. 24.11a–e** Illustration of the point spread function (PSF), which describes how one infinitesimally small point in the source object will be spread out (blurred, smeared) by the imaging system. Images in (a–d): A very thin wire is positioned perpendicular to the slice plane and imaged. (a) Slice tomogram with an idealized imaging resolution, showing true circular cross section of the imaged wire. (b) Profile of the idealized slice image demonstrating distinct edges at the true wire edges. (c) Real slice tomogram shows blurred edges/edge effects because of the system’s limited resolution. (d) Real image PSF is a smoothed profile across the actual image values. Its full width at half maximum (FWHM) can be used as an indicator for system resolution or image sharpness. From [24.16]. Copyright 1994 by The Minerals, Metals & Materials Society. Used with permission. (e) Two PSFs, A and B, with good separation. If an individual PSF is narrow, less blurring will occur, and the small object should still be discernible. If two PSFs are too close together or have overlap, it may be difficult to discern them from one another (A+B). Courtesy of Scanco Medical AG

bars, blurring at the edges reduces the system’s ability to detect the true contrast difference between these materials, and the MTF becomes some fraction of the original thick bar maximum value. Spatial resolution can be described as the spatial frequency at which the MTF falls below a specified percentage of the maximum, and 10% MTF is often chosen as this threshold (Fig. 24.12).

### Contrast and Noise

**Contrast and Linear Attenuation Coefficient.** Contrast is defined as a relative difference between the linear attenuation coefficient of a feature and the surrounding background [24.16, 17, 75]. It is expressed as a percent difference, as shown in the following equation

$$\text{Contrast (\%)} = \frac{|\mu - \mu_b|}{\mu_{\text{ref}}} \cdot 100\% . \quad (24.14)$$



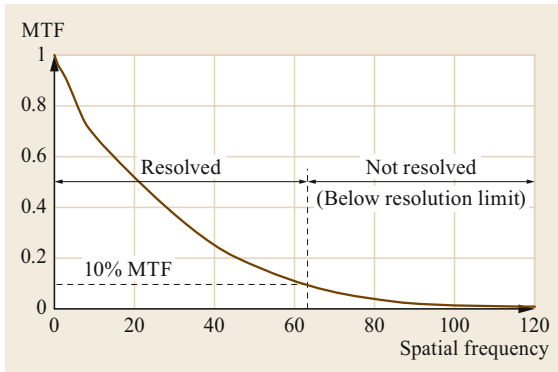


**Fig. 24.12** Modulation transfer function (MTF) is the Fourier transform of the PSF. As objects become smaller and closer together (increased spatial frequency), typically the MTF decreases. At a certain threshold MTF value, usually 10% of the maximum, the object is considered to be under the spatial resolution and therefore not resolved. This threshold generally correlates well with average visual inspection by eye. Courtesy of Scanco Medical AG

In this equation,  $\mu$  is the linear attenuation coefficient of the feature of interest,  $\mu_b$  the linear attenuation coefficient of background, and  $\mu_{\text{ref}}$  the linear attenuation coefficient of a reference material, usually set as the background material, but can be the maximum coefficient for background or reference materials if the background material is air or something with a very low value.

Linear attenuation coefficient values (units of  $1/\text{cm}$ ) are a function of the physical density of the material, the atomic number of the material, and the effective energy of the x-rays coming in contact with the object. In order for features to be detected in a microCT scan, they must have high enough relative contrast.

**Contrast Sensitivity and Noise.** Contrast sensitivity is the system's ability to discriminate between two materials that have low relative contrast difference [24.16, 17, 75]. This is directly related to the signal-to-noise ratio (SNR)

$$\text{SNR} = \frac{N}{\sqrt{N}} = \sqrt{N}, \quad (24.15)$$

where  $N$  is the average number of photons detected per measurement and  $\sqrt{N}$  the standard deviation of the number of photons detected per measurement.

Because the beam intensity being measured consists of a finite number of photons, repeated measurement will always contain some random variation in the number of photons detected. The fewer the number of photons detected, the lower the SNR. This detection

variation is also referred to as quantum noise (or mottle) and is inherent with any system, even if the detector is modeled as an idealized device. Because no detector electronics are perfect, these components also add more quantum noise to the system. Other sources of additional noise include the data acquisition electronics, round off errors in the computational processing steps required in image reconstruction, and noise contained in the reference measurements used to normalize scan projection data.

**Increasing the SNR and Reducing Noise.** Image noise can be a primary limiting factor in distinguishing lower-contrast structures and in accurately representing very small higher-contrast features. Thus, it is the aim of detector designers (as well as researchers) to minimize noise and maximize signal detection.

Any factors that can increase the number of photons detected generally have the effect of reducing noise. Some of the factors that influence the number of photons detected:

- Source intensity (higher intensity = more photons)
- Source-to-detector distance (larger distance = more photons detected)
- Beam collimation (less collimated = larger scanned slice thickness = higher number of photons detected)
- Overall efficiency of the detector.

The overall efficiency of the detector is determined by the geometrical, absorption, and conversion efficiencies. Geometrical efficiency increases with increased number of detectors and detector aperture width. Absorption and conversion efficiencies depend on design parameters of the detector, including size and material composition. Scanned slice thickness is also affected by detector design, and the number of photons detected is directly proportional to scanned slice thickness [24.17].

There can be some complexity in noise reduction tactics. For example, a certain amount of detected signal is scattered radiation, and this reduces contrast by creating additional background noise. Reducing scatter, with tight collimation (resulting in thinner scanned slices) or increasing the object-to-detector distance (which also increases source-to-detector distance), reduces this contribution to noise. However, adjusting these parameters may contribute to additional loss of signal in other ways [24.16, 17, 75].

### Artifacts

There can be systematic variations that result in the appearance of image features that do not correspond to actual structures in the object, and these are categor-

ically called artifacts [24.83, 84]. Generally, there are two primary causes of microCT image artifacts: the finite number of measurements that create a finite amount of data for producing the reconstruction; and imperfections and errors in the hardware and reconstruction processes [24.85].

**Aliasing.** Aliasing artifacts are a result of insufficient sampling of small detailed features due to either too few detector elements or too few view angles or projections [24.16, 17, 83, 84]. This can appear in the images as a series of coarsely spaced weave-like patterns. Aliasing can also present itself as radial streak-like patterns that are apparent either at the outer edges or emanating from a high-contrast structure in the object (Fig. 24.13a).

One way to minimize these effects, especially for the latter, is to use more projections per acquisition rotational view. Aliasing effects can also be a result of reconstructing images at a pixel spacing much larger than the finely sampled projection data. To minimize these effects, selection of a more appropriate reconstruction filter function must be done to filter out spatial frequencies that are higher than that of the reconstructed pixel matrix.

**Beam Hardening.** As mentioned previously, the x-rays produced for microCT imaging have a range of photon energies up to the maximum energy designated. Lower-energy, or soft, photons do not penetrate as well and are attenuated to a greater degree by an object than the higher-energy photons. Thus, the effective energy passing through different sections of the object will vary depending on the thickness at that section. This means that lower-energy photons are preferentially absorbed near the surface, and in reconstructed images the effect will appear as artifactually low linear attenuation coefficient values toward the center of a large uniform object compared to higher values at its periphery [24.16, 17, 83, 84]. Beam-hardening effects are also extremely prevalent in association with slices where metallic objects are present. Metallic objects can produce image quality problems (Fig. 24.13b) that can be attributed to several of the sources listed in this section, but beam hardening is a primary source of image artifacts in the vicinity of these specimens.

The effects of beam hardening can sometimes be mitigated with filtration, but more typically for microCT systems, compensation for the effect is accomplished through software processing. Single-material beam-hardening corrections are relatively simple, particularly if the material being scanned has previously measured transmission data. In general practice, the scanned material will be assumed to have similar char-

acteristics of a material with known calibration data, and a set of beam-hardening correction factors will be utilized based on that assumption. With some objects, such as metallic specimens, available correction processes may not be sufficient to overcome the effects.

When an object is a composite with widely varying effective atomic numbers, the corrections are more difficult. In cases where the object is composed of two distinct materials that are easy to identify from one another, an iterative beam-hardening correction process can be used. For more complex composites, dual-energy techniques can be utilized to provide corrections based on the relative attenuation effects for each material.

**Scatter.** Scattered radiation produces a falsely high detected signal that is not consistent with the actual intensity measured along the beam path. The contribution of scatter in typical systems is relatively low, but even low levels of scatter could present problems due to the high degree of sensitivity required in microCT imaging. The effects are more significant for highly attenuated rays because the scatter signal is relatively large. The additional scattered photons detected can produce image artifacts similar in appearance to beam-hardening artifacts. They can also cause broad bands of low linear attenuation coefficient between high-density structures in the object [24.16, 17, 83, 84].

MicroCT system hardware can be designed to minimize detected scatter radiation. This can be accomplished through the use of tight collimation, increased object-to-detector distance, or directionally sensitive detectors.

On the software processing side, basic beam-hardening corrections typically provide some compensatory effect for scatter detection. However, contrary to beam-hardening effects, dual-energy processing does not provide any benefit in eliminating scatter radiation effects. Specific scatter radiation modeling can also be performed to provide more precise corrections.

**Systemic Factors.** Each hardware component within a microCT system has the potential to produce errors and artifacts if not functioning properly [24.16, 17, 83, 84].

X-ray tube sources are typically highly stable and include feedback control of tube voltage. If variations in tube voltage occur due to degradation of the source or other reasons, the changes would affect output x-ray intensity and effective energy. Variations in effective energy are particularly challenging to correct and may require x-ray source replacement.

Imprecise specimen manipulations (rotations and translations), geometric misalignment of the center of

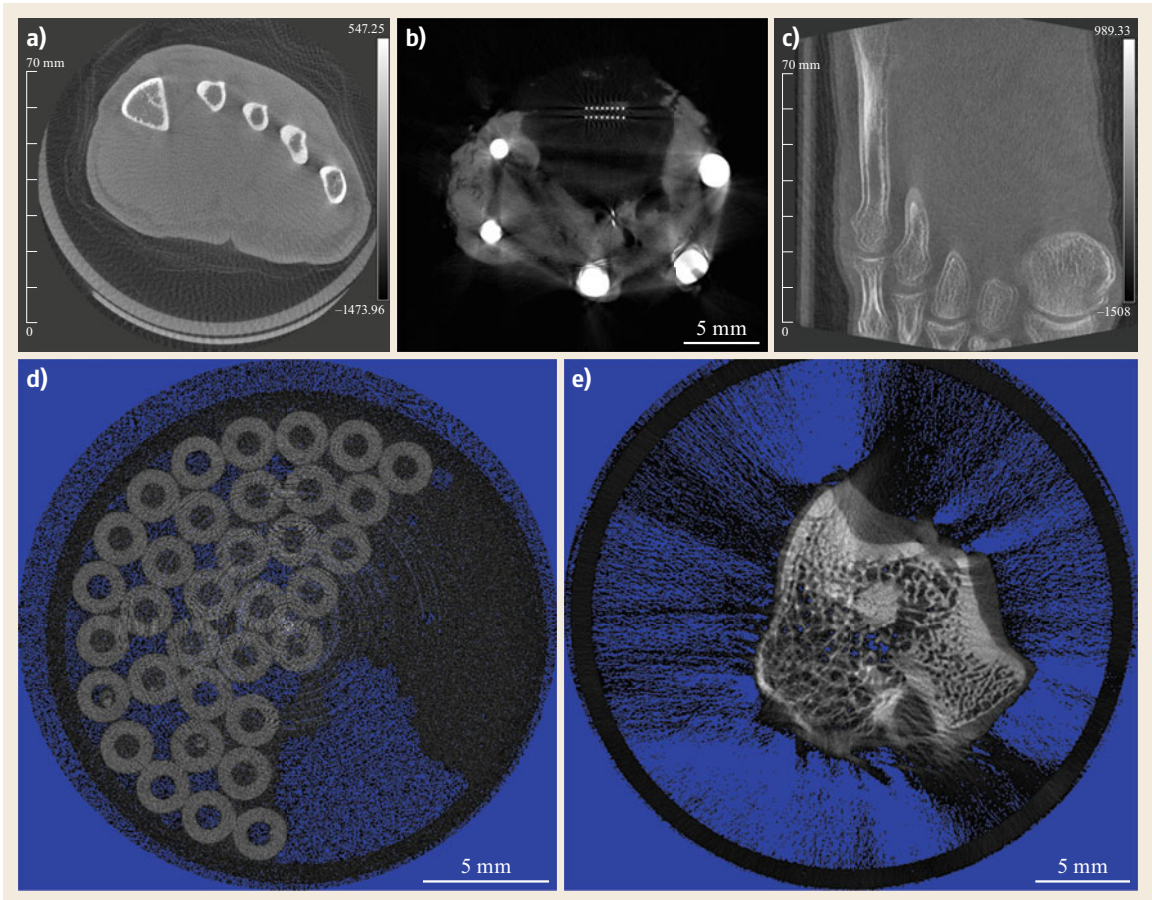


**Fig. 24.13a–e** 2-D slice tomograms depicting various types of image artifacts. **(a)** Aliasing or undersampling, apparent at edges of higher-density bone and around the periphery. **(b)** Metal and beam-hardening artifacts prevalent in the vicinity of large and small metal objects. **(c)** Centering-related systematic ghosting artifacts, apparent around the bone surfaces. **(d)** Ring artifacts. **(e)** Motion artifacts—streaking and star-like patterns

rotation, or improperly characterized position can cause errors in the resulting image reconstruction that appear as blurs, slightly offset ghost images (Fig. 24.13c), streaks, or star-like patterns.

Detector problems can come in the form of non-linear performance across the detector’s dynamic range or degradation or inconsistencies in detector elements. Instability in detector performance may create measurement errors that appear as streak artifacts or ring artifacts in the reconstructions. Well-defined streaks of high or low intensity occur when a single detector element at a particular projection angle provides an anomalous readout. This artifactual measurement is amplified across the slice image during the reconstruction process. Ring artifacts are produced when a single detector element reads slightly high or low relative to its neighboring elements. Because the object rotates relative to the source and detector, a sin-

gle detector element corresponds to a fixed radius in the resulting reconstructed image. The slight measurement difference therefore creates a ring at that radius (Fig. 24.13d).

**Motion.** Non-controlled motion with respect to the source and detector during measurement is a major problem. Because data are collected along many projection paths, precise compilation of these data are essential to creating an accurate reconstructed image slice [24.16, 17, 83, 84]. The source of motion could be imprecise control of the specimen movement components, but it is more likely due to actual movement of the object with respect to the scanner’s hardware components. An object could shift or vibrate if fixed improperly within the specimen holder. If the object undergoes internal changes (e. g., phase shift, fluid flow within the sample, contraction due to drying) over the

course of the scan time, motion artifacts may result. These could take the form of blurring, streaks, or star-like patterns (Fig. 24.13e).

**Partial Volume.** Partial volume artifacts can occur when part of a beam ray passes through one material while another part of the ray passes through another material or background. Scenarios that cause this include rays that are tangential to high-contrast object boundaries, objects that protrude only partly into the measured slice thickness, or an object that transitions in size rapidly in the direction normal to the slice plane [24.16, 17, 75, 83, 84]. Inconsistencies between the measured projection data of the views can become significant enough to produce streaking or shading artifacts, particularly if the two materials have considerably different linear attenuation coefficient values.

One method for reducing partial volume artifacts is to decrease the effective ray size by using a smaller slice thickness and a narrower effective aperture. Some reconstruction filters can also be applied to reduce the sensitivity to these effects. Reducing the contrast difference between the materials can also be effective, and this can be done by immersing the dense material in something with a more similar linear attenuation coefficient.

The partial volume-effect also describes a different volume-averaging process. Each voxel may contain multiple materials; thus volume averaging of the linear attenuation coefficients for each material must be performed to determine the value that the voxel will possess in the reconstructed image. This can result in ar-

tifactual values assigned to certain voxels, particularly if those voxels contain very small high-density features or if they are near the surface of a large, high-density feature.

### Effects of Sample Preparation

The storage and preparation of the sample may affect the resulting image quality and further image analysis. If a specimen is not provided with enough stabilization within a rotating sample holder, there may be motion of the sample with respect to the source beam that would result in motion artifacts in the reconstructed images (Fig. 24.13e). If a specimen typically requires hydration to retain its morphology or is prone to becoming desiccated over time, efforts must be made to keep humidity high within the sample holder. Otherwise, the specimen may experience microscale movement due to drying. Alternatively, the sample may need to be kept submerged in liquid or media during scanning. In this case, the user should be aware that discerning the specimen boundaries may be impossible, depending on the specimen's radiodensity compared to that of the surrounding liquid. The position of the specimen affects the resulting axial slice orientation; thus it may be important for specimens to be positioned in an orientation that will allow the resulting slice orientation to be easily related to the actual specimen. These are some examples of the effects that sample preparation may have. Following consistent procedures for preparing specimens, positioning, and securing them for scanning is important not only for image quality but for streamlining the imaging and analysis procedures.

## 24.4 Quantitative Analyses and Advanced Post-Processing Methods

### 24.4.1 Segmentation

Reconstruction processes output grayscale 2-D slice images or tomograms. To generate quantitative data and 3-D renderings, the user must further process the 2-D grayscale slices via segmentation. Each voxel in each 2-D slice image possesses a linear attenuation coefficient value. Segmentation is the process by which the total volume of voxels is partitioned such that meaningful groupings of voxels within the scan are formed. This often means separating an object (or objects) of interest from the background or from other objects.

There are many segmentation methods. If the linear attenuation coefficient distributions of two objects are very different, a fixed global thresholding technique can provide successful, simple intensity-based segmentation of the objects. If the distribution of linear attenuation coefficient values for the two objects are similar

or overlap, or if structures vary greatly in size across the object, other more complex techniques such as adaptive and active thresholding or contouring [24.86–90] may be necessary to produce the best segmentation of the object(s). Some laboratory microCT systems have corresponding proprietary software that is capable of providing intensity-based or other segmentation processes, and various third-party software algorithms are also available to perform segmentations and image analyses.

One common approach for performing segmentations involves the selection of inclusion regions in each slice using hand-drawn, semi-, or fully automated shapes or contours (Fig. 24.14b). These contours can be used to specifically separate the desired object(s) from background or noise. Additionally, contours can be used to create an outer total volume boundary and within these boundaries apply intensity-based segmentation of one or more materials (Fig. 24.14c–e). After



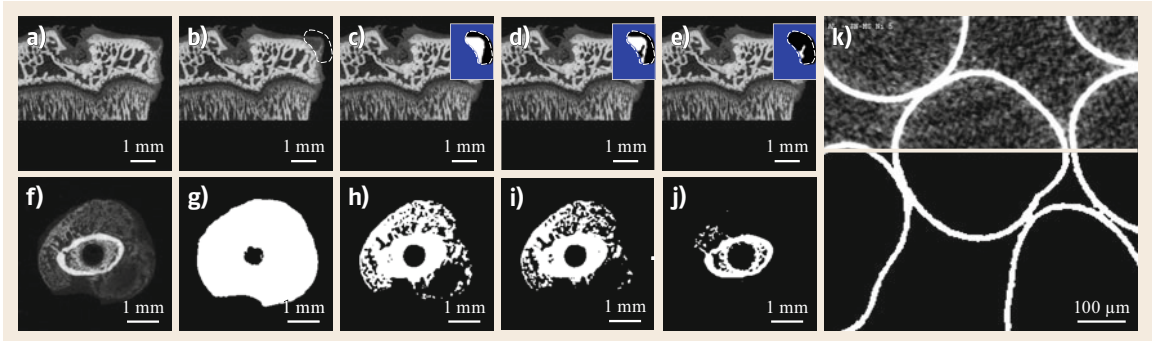


**Fig. 24.14a–k** Image segmentation examples using 2-D slice tomograms, scans performed with Scanco Medical  $\mu$ CT40 ((a–e): 45 kVp; (f–j): 55 kVp) and  $\mu$ CT50 (k: 90 kVp), voxel sizes ranging from 5–16  $\mu$ m. Images in (a–e) taken from coronal slices of a rat proximal tibia, used in marginal osteophyte analysis in osteoarthritis characterization studies, to demonstrate use of contours for segmentation. (a) Original 2-D grayscale slice. (b) Slice image with contour (*dashed white shape near top right*) drawn to designate an outer boundary for the volume of interest. (c) Threshold range applied to provide segmentation for all tissue within the contour. (d) Threshold range applied to provide segmentation of soft tissue only. (e) Threshold range applied to provide segmentation of mineralized tissue only. Images in (f–j) taken from axial slices of a mouse femur with fracture callus, used in assessing fracture healing, to visually demonstrate the effects of threshold choice on segmentation output. (f) 2-D grayscale slice image with no threshold applied. (g) Low threshold range chosen—includes all tissue in the callus, mineralized and non-mineralized. (h–j) Increasingly higher threshold ranges chosen, demonstrating fewer voxels included in the segmentation for (j) compared to (i) compared to (h). (k) Example of visual threshold assessment within a slice, from a cylinder of sintered metal tubes. *Top section* shows the original grayscale and *bottom section* has a segmentation threshold applied. This technique can be used to visually compare grayscale and thresholded object surfaces at the top/bottom section boundary in order to make adjustments to reach visual agreement between the two during the threshold selection process

segmentation processes are performed, one can quantify voxel-based parameters within the designated region, such as object volume, object/total volume ratio, and average linear attenuation coefficient.

Resulting quantitative geometry and radiodensity measurements based on segmentation of one or more 3-D objects from background and noise are dependent on the accuracy of the segmentation parameters to replicate the true 3-D object(s). Selection of standardized segmentation parameters should be done with careful forethought in order to avoid creating artifactual variations in the outcome measures or reducing the sensitivity to detect effects [24.69, 91–93]. Figure 24.14g–j qualitatively demonstrates that at various threshold ranges, visual differences can be observed in the voxels that are retained. An additional factor that may require consideration in the segmentation process is the effect of partial volume averaging at the surfaces of an object. To minimize these effects, some segmentation procedures may include options for eliminating a certain number of surface voxels during the computation of geometry parameters or linear attenuation.

### 24.4.2 Quantitative Capabilities

The initial biomedical application for laboratory microCT imaging was in the quantification of trabecu-

lar bone morphometry. Thus, various algorithms were designed and continue to be the gold standard for producing volumetric, model-independent measures of parameters such as trabecular thickness (Tb.Th), trabecular spacing (Tb.Sp), trabecular number (Tb.N), connectivity, structure model index (SMI), anisotropy, and bone mineral density [24.6, 47, 55–58, 60–63, 65, 66, 94, 95]. Figure 24.15 demonstrates the capability of these algorithms to generate pseudocolor 3-D segmentations (Fig. 24.15a–c) and quantitative measurements for trabecular bone (Fig. 24.15d–g) in mouse distal femoral metaphyses. Additionally, techniques have been developed to characterize cortical and trabecular cracks and their initiation and propagation [24.58, 64, 96]. Quantitative trabecular and cortical bone analysis methods were extended for use in other biomedical applications including morphometric and compositional analyses of soft tissues such as cartilage and vascular networks [24.68–73].

### 24.4.3 Image Export and Further Analyses

Makers of laboratory microCT scan systems generally have system-specific proprietary software for scanner controls, reconstructions, and image processing. Most also have means of converting native 2-D slice image formats to those readable with other software, such

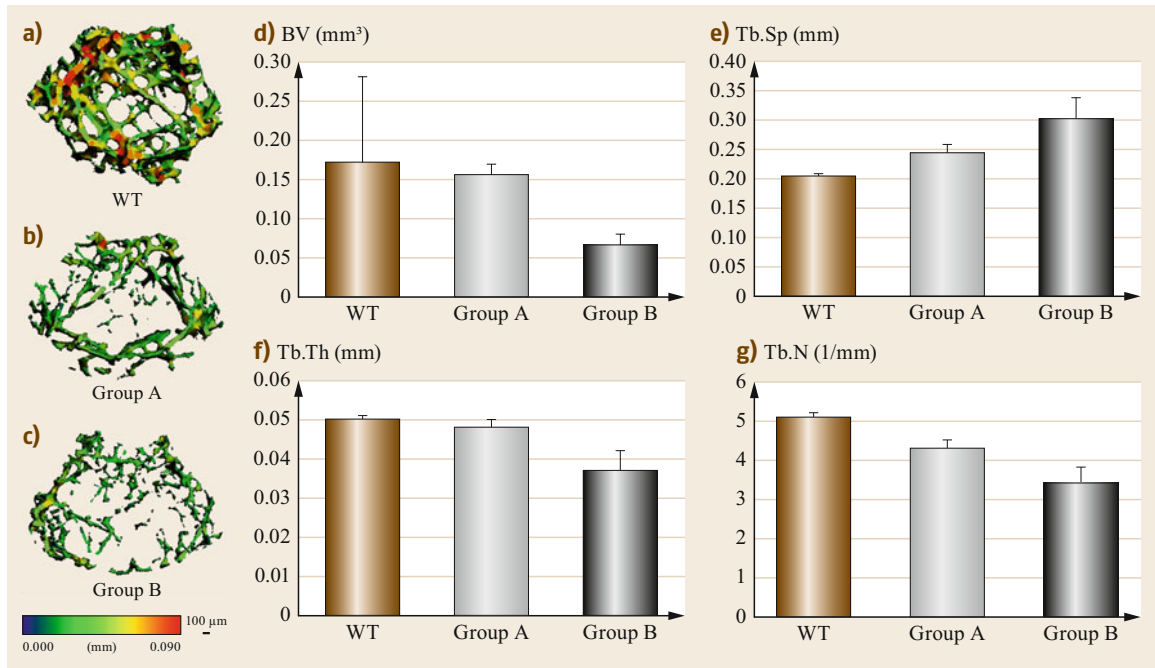


**Fig. 24.15** (a–c) Examples of 3-D pseudocolor thickness map images and (d–g) quantitative bone morphometry data from trabecular bone in mouse femoral metaphyses, immediately distal to the growth plate (scans performed on a Scanco Medical  $\mu$ CT40, 55 kVp, voxel size 12  $\mu$ m). Pseudocolor scale shown in (a–c) indicates red = thicker trabeculae, green/blue = thinner trabeculae. Quantifications for wild type (WT), experimental group A, and experimental group B for (d) bone volume (BV, mm<sup>3</sup>), (e) average trabecular spacing (Tb.Sp, mm), (f) average trabecular thickness (Tb.Th, mm), and (g) average trabecular number (Tb.N, 1/mm). These and other bone morphometry computations were performed via well-established direct-distance transformation methods [24.55–58, 60, 62, 63, 65]

as NIH ImageJ/Fiji or MathWorks Matlab (TIFF, DICOM, etc.). Conversion to 3-D image meshes can also be performed to generate geometries that can be used in finite element (FE) modeling approaches. The ability

to export these images for use in third-party software packages vastly opens the possibilities for further quantitative analyses of data obtained through microCT imaging.

## 24.5 Other Variants and Recent Developments

### 24.5.1 Synchrotron

MicroCT with synchrotron x-radiation offers advantages based on the x-ray source characteristics, advantages which can offset the inconvenience of travel or of scheduling constraints. First, the x-ray beam is very bright, that is, the number of photons per unit time per unit area per unit solid angle is orders of magnitude higher than from tube sources. Data collection rates can be very high compared to lab microCT systems. The beam is highly parallel, and parallel beam reconstruction algorithms are the rule. Second, the storage ring provides a range of x-ray energies, and monochromatic

radiation is typically selected (via monochromator or multilayer optics) to optimize contrast within the sample. Some instruments can switch to imaging with polychromatic radiation, an advantage for highly absorbing specimens or for real time or in operando imaging (Sect. 24.5.8). Third, the source at many beam lines has enough spatial coherence for x-ray phase contrast microCT (Sect. 24.5.4), a family of approaches allowing discrimination of materials with nearly identical linear attenuation coefficients, e. g., different soft tissue types or different polymers.

Synchrotron microCT instruments are spread throughout the world, and their capabilities differ

enough that the typical characteristics listed here may be somewhat inaccurate for a specific facility. In general terms, these instruments are designed to image fields of view of 0.5–5 mm rather than sample diameters  $> 1\text{--}2\text{ cm}$  and to operate with energies  $8 \leq E \text{ (keV)} \leq 35$ . It is routine to collect projections for high-resolution/high-sensitivity reconstructions (voxel size  $\leq 1\ \mu\text{m}$ , contrast sensitivity approaching 12 bits, i. e.,  $4 \times 10^3$  gray levels,  $(2\text{K})^3$  voxel volumes) in about 10 min. At some facilities, voxel sizes can be substantially below  $0.5\ \mu\text{m}$ . These instruments run around the clock, and data collection rates  $> 1\text{ TB/day}$  are common. Most facilities have computational facilities powerful enough to reconstruct data at this rate, but input/output speeds can be limiting. A more significant bottleneck is interrogating and interpreting the data. Synchrotron microCT reconstructions with absorption contrast appear in Figs. 24.3a, 24.4e, 24.16, and 24.18a,c

If the sample cross section is somewhat larger than the imaging field of view with the required voxel size, one can:

1. Perform local tomography (center the field of view on the region of interest and ignore the mass outside this region, mass that rotates in and out of view), see Fig. 24.16a–c
2. Offset the rotation axis from the sample center and record views over  $360^\circ$  rotation instead of  $180^\circ$  (the effective field of view is now larger than the detector width, see [24.77] for diagrams), e. g., Fig. 24.16d,e
3. Stitch together radiographs from adjacent positions and use the composite views for reconstruction.

Figure 24.16a shows a slice of a sea urchin jaw imaged in situ, that is within the test or mineralized body which is out of the field of view; the enlargements of Fig. 24.16b,c show the soft tissue esophagus and one of the five teeth, respectively. Figure 24.16d is a slice of a human second metacarpal bone; and the fine porosity of this bone is visible in the enlargement of Fig. 24.16e. Figure 24.16f shows a 3-D printed sample of four bars of a polymer binder and two different hydroxyapatite powders; diffraction tomography of this sample is shown in Sect. 24.5.7.

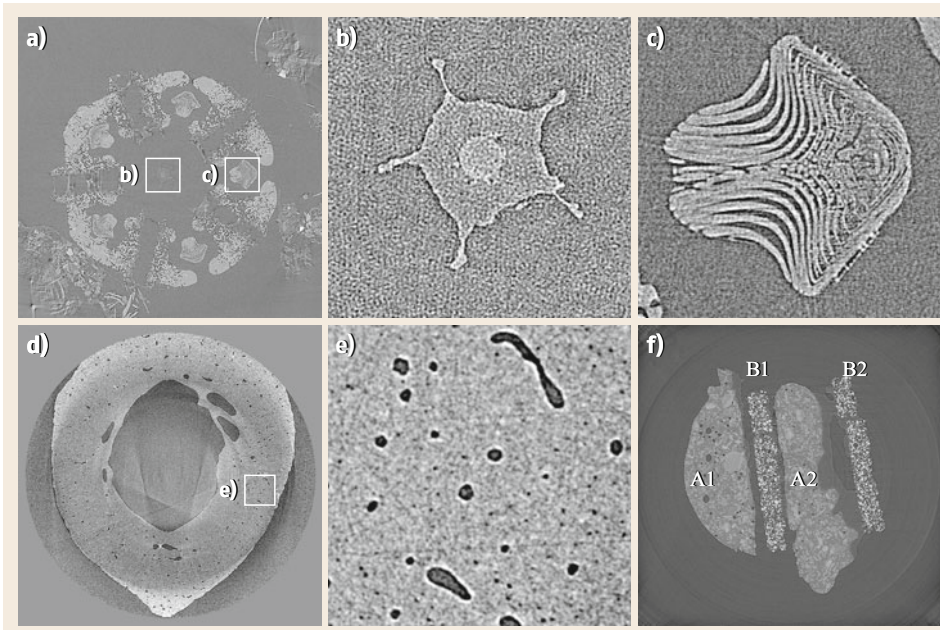


**Fig. 24.16a–f** Synchrotron microCT data from beamline 2-BM, APS. The lighter the pixel, the more absorbing the corresponding voxel. **(a)** Sea urchin jaw consisting of calcite and soft tissue. Field of view  $2048 \times 2048$  voxels;  $1.45\ \mu\text{m}$  voxels; energy  $E = 22.5\ \text{keV}$ . Local tomography. Enlargements of **(b)** the esophagus (soft tissue) and **(c)** tooth. Courtesy of S.R. Stock, A. Ziegler, and X. Xiao. **(d)** Slice at mid-diaphysis of human second metacarpal bone. Note that the upper portion of the bone is out of view. Field of view  $3235 \times 3235$  voxels;  $2.9\ \mu\text{m}$  voxels; polychromatic radiation. **(e)** Enlarged area of the metacarpal bone showing porosity. Courtesy of S.R. Stock and C. Soriano. **(f)** Additive manufactured specimen of hydroxyapatite + polymer in the form of two pairs of bars; bars A and B have different powder types. This sample was also studied with diffraction tomography (see Sect. 24.5.7, Fig. 24.19, and [24.97]). Field of view  $2048 \times 2048$  voxels;  $1.45\ \mu\text{m}$  voxels; energy  $E = 27.2\ \text{keV}$

### 24.5.2 NanoCT

For researchers seeking to extend imaging capabilities beyond the spatial resolution reached by microCT, the development of nanofocus x-ray tube systems with efficient condenser optics allows focal spot sizes to be decreased and spatial resolution to be increased to the sub-micron level. With synchrotron radiation, spatial resolution can even be pushed to below 100 nm. There are currently only a few commercially available versions of laboratory nanoCT systems, including the GE phoenix nanotom s, the Bruker SkyScan 2211, and the Zeiss Xradia Ultra models. Many synchrotron facilities have nanoCT capabilities, but access to these is more limited than for microCT beamlines [24.66].

### 24.5.3 In Vivo Imaging

The first in vivo imaging performed with a microCT system (also referred to as x-ray tomographic microscopy, or XTM, at the time) occurred in the mid-1990s with quantification of rat trabecular bone morphometric indices [24.98, 99]. Soon afterwards, synchrotron radiation was utilized to perform in vivo scans of trabecular bone ultrastructure at a range of resolutions, including 1–2  $\mu\text{m}$ —high enough resolution to allow for assessment of features such as resorption cavities [24.100]. One major concern in the early development of in vivo microCT imaging was the effect of radiation dose experienced by small animals. Advancing systems toward providing low radiation doses, maintaining short scan times, and developing respiratory and cardiac gating techniques [24.101] has made in vivo microCT imaging a powerful method for collecting longitudinal quantitative measurements in

animal models of disease, degeneration, and regeneration. One of the predominant current applications of in vivo laboratory and synchrotron microCT imaging has been for trabecular and cortical bone-related quantifications [24.43, 64, 102]. However, microCT has also been used to visualize and evaluate vasculature, cardiopulmonary function, gastrointestinal systems, other organs, and tumors in live animals using contrast agents and nanoparticles [24.72, 103–108]. Figure 24.17 shows examples of 2-D and 3-D images obtained using in vivo microCT techniques for rodents.

### 24.5.4 Phase Contrast

Equations (24.1) and (24.2) incompletely describe x-ray attenuation, but they suffice for most applications. These equations do not consider refraction of the x-rays when they traverse solids and liquids. Indices of refraction differ from one by a few parts per million, and small changes in electron density between different materials (say different polymers or soft tissues) is enough to distort x-ray wavefronts which pass through regions of different electron density. The more complete description is needed when imaging with a spatially coherent beam, obtained with (a) an x-ray tube with a very small focal spot or with slits providing a small virtual source size or (b) synchrotron radiation from some (but not all) storage rings.

There are several approaches obtaining phase contrast radiographs and using them for reconstructions whose contrast is based on x-ray phase rather than absorption differences. In the propagation method, the detector is placed much farther away from the sample as is normal for absorption contrast imaging ( $\approx 1\text{ m}$  versus  $\approx 1\text{ cm}$ ); refracted x-rays diverge and interfere

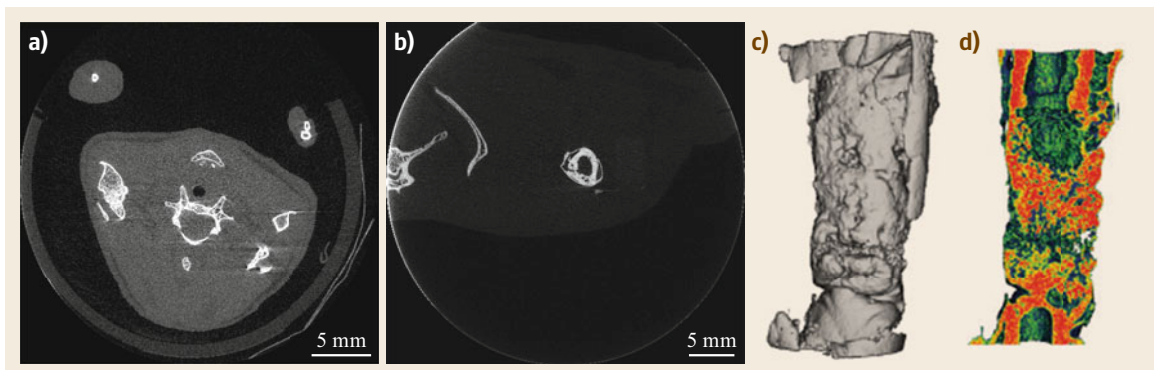


**Fig. 24.17a–d** In vivo microCT imaging examples, scans performed with a Scanco Medical vivaCT40, 55 kVp, voxel sizes ranging from 15–38  $\mu\text{m}$ . **(a)** Mouse axial slice tomogram (displays vertebrae and long bones of the legs). **(b)** Rat axial slice tomogram (displays pelvis and femur). Rat femoral segmental defect healing model, **(c)** 3-D binarized segmentation of the full defect volume of interest and **(d)** mineral density pseudocolor mapping (*red* = higher density, *green* = lower density) subsectioned along the long axis of the defect



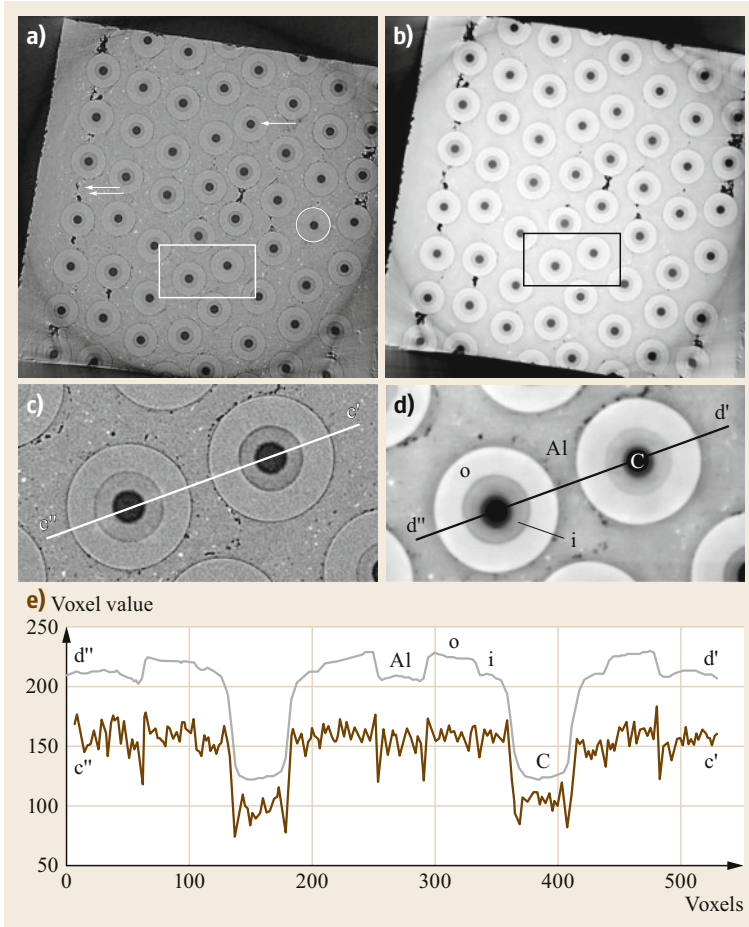
with other x-rays at the detector plane producing detectable fringes in the image at external and internal boundaries between materials with different electron densities. Phase is recovered either by using radiographs acquired at four or more specimen—detector separations (typically from 5 mm to 1 m or more) or by using a single large separation and the Paganin algorithm [24.110, 111]. In diffraction-enhanced imaging, an analyzer crystal is placed in the x-ray beam after the sample; images recorded with different settings of the analyzer isolate changes in the phase angle by selecting only a small angular fraction of the refracted radiation. The grating (Talbot) interferometry method translates one analyzer grating relative to a second in order to provide sensitivity to x-ray phase. Crystal interferometers are also used for phase tomography.

Figure 24.18 compares absorption versus phase slices of an Al/SiC monofilament composite (single-distance propagation approach). Note that the linear attenuation coefficients of Al and SiC differ little, and phase contrast provides greater visibility of Al and SiC

as well as the two main microstructural zones in the SiC monofilaments.

### 24.5.5 Dual Energy

One limitation of single-energy microCT is distinguishing two materials that have linear attenuation coefficient values that are too similar to be separated through simple intensity-based segmentation. Dual-energy microCT techniques rely on producing measurements at one energy where the photoelectric effect dominates and one energy where Compton scattering dominates such that relationships can be made to represent atomic number and electron density, respectively. For example, these methods have been used to effectively segment mineralized tissue and contrast-perfused vasculature in a rat specimen [24.112] as well as evaluate cardiac injury in a mouse model [24.113]. This technique, when using synchrotron radiation at energies on either side of the absorption edge of an element of interest within an object, is also particularly use-



**Fig. 24.18a–e** Synchrotron microCT reconstructions of an Al/SiC monofilament composite specimen scanned at  $0.74 \mu\text{m}$  isotropic voxels for demonstration of phase contrast imaging. (a) Absorption contrast. One SiC fiber is circled; a single arrow points to the fiber's carbon core; the double arrow identifies processing voids. The boxed area is enlarged in (c). Recorded with 22 keV x-ray energy. (b) Reconstruction with phase contrast. The boxed area is enlarged in (d). Recorded with 30 keV x-ray energy. (c) and (d) Enlarged area of the same two fibers in (a) and (c), respectively, with solid lines indicating where profiles were measured. Inner i and outer o SiC microstructural zones are much more visible in the phase reconstruction, but some of the zones are less distinct (e.g., left versus right fiber) in both phase and absorption reconstructions. Aluminum and even carbon core are more differentiated in the phase reconstruction. (e) Voxel values versus position (from c', d' at 0 to c'', d'' at 530). Note 0–255 scaling. Republished with permission of John Wiley and Sons Inc. [24.109]

ful in studies of fluid partition and flow in porous materials.

### 24.5.6 Fluorescence

X-ray fluorescence CT (XFCT) and fluorescence molecular tomography (FMT) combined with conventional microCT have emerged as techniques that can extend CT capabilities to the molecular level. Particularly, these systems can be used to detect in vivo fluorescence emissions from nanoprobe such as functionalized gold nanoparticles (GNPs) or near-infrared (NIR) proteins. With exposure to high-energy x-rays, the energy change that occurs when electrons are displaced and vacancies in atoms are filled is elementally specific. Thus, the fluorescent energy measured during this process is unique for each element, and the proportion of each element present in the scanned sample can be quantified using image analysis software. Nanoparticles or nanoprobe can be targeted to enable imaging of molecular events, biological processes, and tissue vascularity, with notable applicability in tumor detection and cancer therapies [24.114, 115].

### 24.5.7 X-Ray Scattering Tomography

In addition to absorption and refraction, x-rays are scattered by the atoms within the sample, and this signal can be used as the input for reconstruction. The resulting slices map x-ray scattering-related quantities instead of linear attenuation coefficient or x-ray phase. This approach has received limited attention until about 10 years ago, but since then has been used in materials as diverse as bone and concrete [24.116]. Apparatus for scattering tomography employ synchrotron x-radiation and first-generation geometry (pencil beam and translate-rotate data collection, Fig. 24.19). Collection of data for reconstructing a slice is much slower than for attenuation tomography because of the experimental geometry and of the small fraction of scattered x-rays that reinforce and can be collected with a detector. One result is that the voxel size is typically much larger than is typical for absorption microCT with synchrotron radiation.

X-ray scattering occurs in all directions, and, if the sample contains crystalline material, this scattering reinforces in certain directions described by Bragg's law which relates reinforced scattering directions  $2\theta$  to crystal periodicities, the x-ray energy, and orientation of the incident beam [24.82]. The reinforced scattering is termed diffraction and occurs in the wide-angle x-ray scattering (WAXS) regime; these diffraction peaks or reflections  $hkl$  typically correspond to crystal periodicities ( $d$ -spacings)  $0.5 \leq d(\text{\AA}) \leq 8$ . The grains within

polycrystalline specimens have many different orientations, and cones of diffracted intensity result, with each  $d$ -spacing producing a different cone centered on the incident beam. As shown in Fig. 24.19a, the cones are recorded as a series of rings of higher intensity on the area detector. Small-angle x-ray scattering (SAXS) occurs at much smaller angles than WAXS and can also be used in tomographic reconstruction, e. g., peaks from the collagen D-period in bone or dentin.

The simplest reconstruction strategy is to use the integrated intensity of each  $hkl$  peak in the diffraction pattern (Fig. 24.19b). The variation of  $hkl$  integrated intensity versus position for a single angle comprises one view, and the series of views are used for reconstruction much like the absorption profiles are used for conventional microCT. Typically, slices are reconstructed for different  $hkl$ ; if the rings are from different crystallographic phases, the resulting reconstructions will show the spatial distribution of these phases; and the transmitted beam intensity is also measured (ion chamber in Fig. 24.19a), producing a slice with attenuation contrast [24.117].

A more detailed approach entails reconstructing slices using the intensity within each  $2\theta$  annulus regardless of whether the intensity is greater than background. If there are  $N$  such annuli in the pattern, then one obtains  $N$  slices. Note that the positions within these  $N$  slices are exactly registered. Then, for each position  $x, y$ , one can take that voxel's intensity from each of the  $N$  slices and recombine this information in a plot of intensity versus  $2\theta$  (or equivalently, intensity versus  $d$ ). In other words, one obtains a diffraction pattern from each voxel within the slice. Fig. 24.19c compares diffraction patterns for two positions within the sample shown in Fig. 24.16f): one pattern from one of the A bars (nanocrystalline hydroxyapatite) and one from a B bar (much larger crystallites of hydroxyapatite) [24.97]. The former diffraction peaks are expected to be much broader than the latter (see [24.82]), and this is what is observed in the reconstructions. The diffraction patterns for each voxel can also be used to produce maps of lattice parameters within the slice (Fig. 24.19d). Further, reconstructions with different azimuthal sectors of the diffraction rings can be used to provide maps of crystallographic texture, that is, fractions of crystal volume in different orientations [24.97].

### 24.5.8 In Situ/In Operando/Real-Time Tomography

The power of microCT is most evident when one repeatedly interrogates the volume of a sample as it changes. Here, the sample acts as its own control via comparison of subsequent stages with the initial

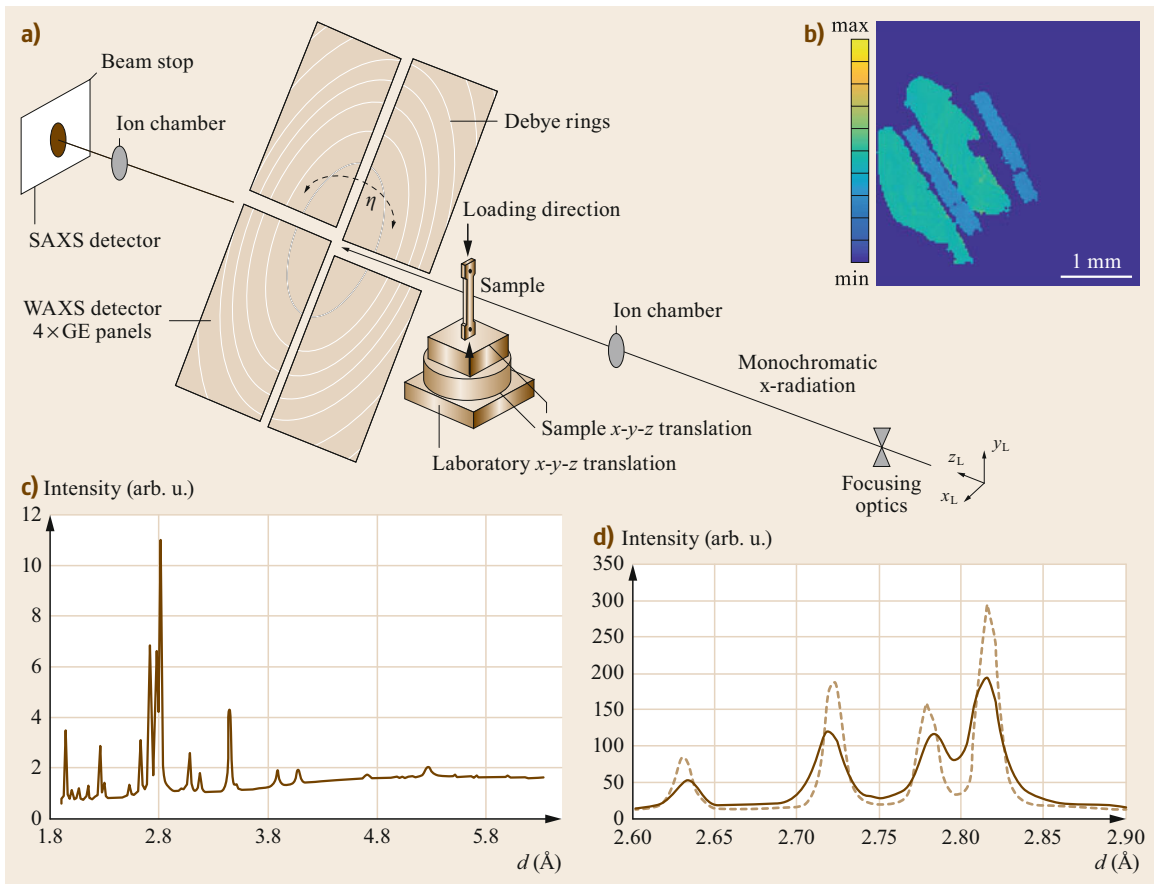


**Fig. 24.19** (a) X-ray scattering tomography experimental arrangement at 1-ID, Advanced Photon Source (APS, Argonne National Laboratory, University of Chicago). Data in panels (b–d) are for the hydroxyapatite sample shown in Fig. 24.16f and are adapted from [24.97]. (b) Azimuthally averaged WAXS pattern. (c) 1-D patterns from a position within one of the A bars and within one of the B bars (see Fig. 24.16f). The hydroxyapatite in bars A1 and A2 (solid line) produces broader diffraction peaks and much smaller crystallite size than the material in bars B1 and B2. (d) Reconstruction mapping lattice parameter  $c$  (from Rietveld refinement) over the range  $6.85 \leq c(\text{Å}) \leq 6.95$

structure. This was first exploited in 1989 for in situ microCT crack closure observation in an Al alloy specimen [24.118]; quantification of crack opening as a function of 3-D position and of applied load revealed patterns of contact [24.119]. Soon after the crack closure measurements, different stages of chemical vapor infiltration of a SiC composite were studied [24.120] and included quantification of patterns of channel closure as a function on composite lay-up [24.121].

Since the early in situ studies requiring hours of data acquisition per observation, x-ray sources and detectors have improved to the point where data sets can be collected in substantially less than one second. Some

compromises may be required (smaller number of detector pixels, smaller number of views, lower dynamic range) or detectors with substantial integrated storage or extremely high data transfer rates may be used. Many in operando or real-time studies have appeared and include battery electrolyte and electrode evolution, corrosion, solidification and melting of solids, crack growth, and even rising of bread. Transient but repeated phenomena can be studied by exploiting the temporal structure of synchrotron radiation (the circulating electrons producing the x-rays are grouped into discrete bunches) and using gating similar to that in vivo systems; imaging 3-D fuel sprays is one example.

## 24.6 Summary

This chapter has sought to provide insight on the history, physics, and techniques that form the fundamentals of microCT imaging. There are entire reference texts and many publications devoted to describing individual aspects of this chapter in much more depth, but the intent of the authors is to provide a detailed introduction to the use of microCT

for nondestructive imaging of materials. Practically speaking, the chapter also provides image analysis information, describes potential imaging artifacts, and illustrates many of the current applications in which microCT imaging is being utilized to set standards for generating high-resolution images and quantitative data.

## References

- 24.1 G.N. Hounsfield: A method of and apparatus for examination of a body by radiation such as X or gamma radiation, United Kingdom Patent 1283915 (1968–1972)
- 24.2 S. Webb: *From the Watching of Shadows: The Origins of Radiological Tomography* (IOP, Bristol 1990)
- 24.3 D.K. Bowen, J.C. Elliott, S.R. Stock, S.D. Dover: X-ray microtomography with synchrotron radiation, *SPIE* **691**, 94–98 (1986)
- 24.4 J.C. Elliott, S.D. Dover: X-ray microtomography, *J. Microsc.* **126**(2), 211–213 (1982)
- 24.5 J.C. Elliott, S.D. Dover: Three-dimensional distribution of mineral in bone at a resolution of 15 micron determined by x-ray microtomography, *Metab. Bone Dis. Relat. Res.* **5**(5), 219–221 (1984)
- 24.6 L.A. Feldkamp, S.A. Goldstein, A.M. Parfitt, G. Jenson, M. Kleerekoper: The direct examination of three-dimensional bone architecture in vitro by computed tomography, *J. Bone Miner. Res.* **4**(1), 3–11 (1989)
- 24.7 B.P. Flannery, H.W. Deckman, W.G. Roberge, K.L. D'Amico: Three-dimensional x-ray microtomography, *Science* **237**(4821), 1439–1444 (1987)
- 24.8 J.H. Kinney, Q.C. Johnson, U. Bonse, M.C. Nichols, R.A. Saroyan, R. Nusshardt, R. Pahl, J.M. Brase: Three-dimensional x-ray computed tomography in materials science, *MRS Bulletin* **XIII**, 13–17 (1988)
- 24.9 J.L. Kuhn, S.A. Goldstein, M.J. Ciarelli, L.S. Matthews: The limitations of canine trabecular bone as a model for human—A biomechanical study, *J. Biomech.* **22**(2), 95–107 (1989)
- 24.10 M.W. Layton, S.A. Goldstein, R.W. Goulet, L.A. Feldkamp, D.J. Kubinski, G.G. Bole: Examination of subchondral bone architecture in experimental osteo-arthritis by microscopic computed axial-tomography, *Arthritis Rheum.* **31**(11), 1400–1405 (1988)
- 24.11 P. Spanne, M.L. Rivers: Computerized microtomography using synchrotron radiation from the NSLS, *Nucl. Instrum. Methods Phys. Res. B* **24/25**, 1063–1067 (1987)
- 24.12 J. Hormes, J. Warner: Industrial use of synchrotron radiation: Love at second sight. In: *Industrial Accelerators and Their Applications*, ed. by R.W. Hamm, M.E. Hamm (World Scientific Publishing, Hackensack 2012)
- 24.13 The European Synchrotron: European Synchrotron Radiation Facility, <http://www.esrf.eu/home.html> (2016)
- 24.14 A.L. Robinson: History of synchrotron radiation. In: *X-ray Data Booklet*, 3rd edn., ed. by A.C. Thompson (Lawrence Berkeley National Laboratory: Center for X-ray Optics Advanced Light Source, Berkeley 2009)
- 24.15 O. Brunke, K. Brockdorf, S. Drews, B. Müller, T. Donath, J. Herzen, F. Beckmann: Comparison between X-ray tube based and synchrotron radiation based  $\mu$ CT, *Proceedings SPIE* (2008), <https://doi.org/10.1117/12.794789>
- 24.16 D.C. Copley, J.W. Eberhard, G.A. Mohr: Computed-tomography. 1. Introduction and industrial applications, *JOM* **46**(1), 14–26 (1994)
- 24.17 M.J. Dennis: Industrial computed tomography. In: *Nondestructive Evaluation and Quality Control*, 2nd edn., ASM Handbook, Vol. 17, ed. by ASM Handbook Committee (ASM International, Materials Park 1989)
- 24.18 A.C. Kak, M. Slaney: *Principles of Computerized Tomographic Imaging* (IEEE, New York 1988)
- 24.19 E.L. Ritman: Micro-computed tomography-current status and developments, *Annu. Rev. Biomed. Eng.* **6**, 185–208 (2004)
- 24.20 R.H. Bossi, G.E. Georgeson: The application of x-ray computed-tomography to materials development, *JOM* **43**(9), 8–15 (1991)
- 24.21 T.M. Breunig: *Nondestructive Evaluation of Damage in SiC/Al Metal/Matrix Composite Using X-ray Tomographic Microscopy* (Georgia Institute of Technology, Atlanta 1992)
- 24.22 T.M. Breunig, J.C. Elliott, S.R. Stock, P. Anderson, G.R. Davis, A. Guvenilir: Quantitative characterization of damage in a composite material using x-ray tomographic microscopy. In: *X-ray Microscopy III*, Vol. 67, ed. by A.G. Michette, G.R. Morrison, C.J. Buckley (Springer, Berlin 1992) pp. 465–468
- 24.23 T.M. Breunig, S.R. Stock, A. Guvenilir, J.C. Elliott, P. Anderson, G.R. Davis: Damage in aligned fibre SiC/Al quantified using a laboratory x-ray tomographic microscope, *Composites* **24**, 209–213 (1993)
- 24.24 M.D. Butts: *Nondestructive Examination of Nicalon Fiber Composite Preforms Using X-ray*



- Tomographic Microscopy* (Georgia Institute of Technology, Atlanta 1993)
- 24.25 M.D. Butts, S.R. Stock, J.H. Kinney, T.L. Starr, M.C. Nichols, C.A. Lundgren, T.M. Breunig, A. Guvenilir: X-ray tomographic microscopy of Nicalon preforms and chemical vapor infiltrated Nicalon silicon-carbide composites, *MRS Proceedings* **250**, 215–219 (1992)
- 24.26 Y. Cao, T.D. Wu, H. Wu, Y. Lang, D.Z. Li, S.F. Ni, H.B. Lu, J.Z. Hu: Synchrotron radiation micro-CT as a novel tool to evaluate the effect of agomir-210 in a rat spinal cord injury model, *Brain Res.* **1655**, 55–65 (2017)
- 24.27 C.A. Carlsson, G. Matscheko, P. Spanne: Prospects for microcomputerized-tomography using synchrotron radiation, *Biol. Trace Elem. Res.* **13**(1), 209–217 (1987)
- 24.28 L.R.L. Dollar: *Evaluation of Nondestructive X-ray Techniques for Electronic Packaging Materials* (Georgia Institute of Technology, Atlanta 1992)
- 24.29 J.C. Elliott, P. Anderson, G.R. Davis, F.S.L. Wong, S.D. Dover: Computed-tomography. 2. The practical use of a single-source and detector, *JOM* **46**(3), 11–19 (1994)
- 24.30 G.E. Georgeson, R.H. Bossi: Computed-tomography of advanced materials and processes. In: *Nondestr. Eval. Mater. Prop. Adv. Mater.; Proc. Symp. TMS Annu. Meet., New Orleans* (1991) pp. 99–108
- 24.31 A. Guvenilir: *Investigation into Asperity Induced Closure in an Al-Li Alloy Using X-ray Tomography* (Georgia Institute of Technology, Atlanta 1995)
- 24.32 S.B. Lee: *Nondestructive Examination of Chemical Vapor Infiltration of 0°/90° SiC/Nicalon Composites* (Georgia Institute of Technology, Atlanta 1993)
- 24.33 C.L. Lin, A.R. Videla, Q. Yu, J.D. Miller: Characterization and analysis of porous, brittle solid structures by x-ray micro computed tomography, *JOM* **62**(12), 86–89 (2010)
- 24.34 R. Morano: *Effect of R-Ratio on Crack Closure in Al-Li 2090 T8E41, Investigated Non-Destructively with X-Ray Micro-Tomography* (Georgia Institute of Technology, Atlanta 1998)
- 24.35 S.R. Stock: X-ray microtomography of materials, *Int. Mater. Rev.* **44**(4), 141–164 (1999)
- 24.36 S.R. Stock, A. Guvenilir, T.M. Breunig, J.H. Kinney, M.C. Nichols: Computed-tomography. 3. Volumetric, high-resolution x-ray-analysis of fatigue-crack closure, *JOM* **47**(1), 19–23 (1995)
- 24.37 T. Winkler, X.Y. Dai, G. Mielke, S. Vogt, H. Buechner, J.T. Schantz, Y. Harder, H.G. Machens, M.M. Morlock, A.F. Schilling: Three-dimensional quantification of calcium salt-composite resorption (CSC) in vitro by micro-computed tomography (micro-CT), *JOM* **66**(4), 559–565 (2014)
- 24.38 A.S. Lin, T.H. Barrows, S.H. Cartmell, R.E. Guldberg: Microarchitectural and mechanical characterization of oriented porous polymer scaffolds, *Biomaterials* **24**(3), 481–489 (2003)
- 24.39 S.J. Hollister, R.A. Levy, T.M. Chu, J.W. Halloran, S.E. Feinberg: An image-based approach for design and manufacturing craniofacial scaffolds, *Int. J. Oral Maxillofac. Surg.* **29**(1), 67–71 (2000)
- 24.40 A. Hasan, K.A. Alshibli: Experimental assessment of 3D particle-to-particle interaction within sheared sand using synchrotron microtomography, *Geotechnique* **60**(5), 369–379 (2010)
- 24.41 D.L. Safranski, J.M. Boothby, C.N. Kelly, K. Beatty, N. Lakhera, C.P. Frick, A. Lin, R.E. Guldberg, J.C. Griffiths: Thermo-mechanical behavior and structure of melt blown shape-memory polyurethane nonwovens, *J. Mech. Behav. Biomed. Mater.* **62**, 545–555 (2016)
- 24.42 P. Verma, M.L. Shofner, A. Lin, K.B. Wagner, A.C. Griffin: Induction of autetic response in needle-punched nonwovens: Effects of temperature, pressure, and time, *Phys. Status Solidi (b)* **253**(7), 1270–1278 (2016)
- 24.43 S. Bayat, L. Apostol, E. Boller, T. Brochard, F. Peyrin: In vivo imaging of bone micro-architecture in mice with 3D synchrotron radiation microtomography, *Nucl. Instrum. Methods Phys. Res. A* **548**, 247–252 (2005)
- 24.44 S. Cartmell, K. Huynh, A. Lin, S. Nagaraja, R. Guldberg: Quantitative microcomputed tomography analysis of mineralization within three-dimensional scaffolds in vitro, *J. Biomed. Mater. Res. A* **69**(1), 97–104 (2004)
- 24.45 G.T. Charras: *Digital Image-Based Finite Element Modeling (DIBFEM): Validation and Application to Biological Structures* (Georgia Institute of Technology, Atlanta 1998)
- 24.46 D.W. Dempster, R. Lindsay: Pathogenesis of osteoporosis, *Lancet* **341**(8848), 797–801 (1993)
- 24.47 M. Ding, A. Odgaard, I. Hvid: Accuracy of cancellous bone volume fraction measured by micro-CT scanning, *J. Biomech.* **32**(3), 323–326 (1999)
- 24.48 M. Ding, A. Odgaard, F. Linde, I. Hvid: Age-related variations in the microstructure of human tibial cancellous bone, *J. Orthop. Res.* **20**(3), 615–621 (2002)
- 24.49 K. Engelke, C.C. Gluer, H.K. Genant: Structural and fractal analyses of the trabecular network using micro-computed tomography images, *J. Bone Miner. Res.* **8**, S354 (1993)
- 24.50 K. Engelke, W. Graeff, L. Meiss, M. Hahn, G. Dellinger: High spatial-resolution imaging of bone-mineral using computed microtomography—Comparison with microradiography and undecalcified histologic sections, *Invest. Radiol.* **28**(4), 341–349 (1993)
- 24.51 R.W. Goulet, S.A. Goldstein, M.J. Ciarelli, J.L. Kuhn, M.B. Brown, L.A. Feldkamp: The relationship between the structural and orthogonal compressive properties of trabecular bone, *J. Biomech.* **27**(4), 375–389 (1994)
- 24.52 R.E. Guldberg, N.J. Caldwell, X.E. Guo, R.W. Goulet, S.J. Hollister, S.A. Goldstein: Mechanical stimulation of tissue repair in the hydraulic bone chamber, *J. Bone Miner. Res.* **12**(8), 1295–1302 (1997)

- 24.53 R.E. Guldberg, S.J. Hollister, G.T. Charras: The accuracy of digital image-based finite element models, *J. Biomech. Eng.* **120**(2), 289–295 (1998)
- 24.54 R.E. Guldberg, A.S. Lin, R. Coleman, G. Robertson, C. Duvall: Microcomputed tomography imaging of skeletal development and growth, *Birth Defects Res. C Embryo Today* **72**(3), 250–259 (2004)
- 24.55 T. Hildebrand, A. Laib, R. Müller, J. Dequeker, P. Rüeegsegger: Direct three-dimensional morphometric analysis of human cancellous bone: Microstructural data from spine, femur, iliac crest, and calcaneus, *J. Bone Miner. Res.* **14**(7), 1167–1174 (1999)
- 24.56 B. Koller, A. Laib: Calibration of micro-CT data for quantifying bone mineral and biomaterial density and microarchitecture. In: *Advanced Bioimaging Technologies in Assessment of the Quality of Bone and Scaffold Materials*, ed. by L. Qin, H.K. Genant, J.F. Griffith, K.S. Leung (Springer, Berlin 2007)
- 24.57 J.L. Kuhn, S.A. Goldstein, L.A. Feldkamp, R.W. Goulet, G. Jasion: Evaluation of a microcomputed tomography system to study trabecular bone structure, *J. Orthop. Res.* **8**(6), 833–842 (1990)
- 24.58 A. Laib, O. Barou, L. Vico, M.H. Lafage-Proust, C. Alexandre, P. Rügsegger: 3D micro-computed tomography of trabecular and cortical bone architecture with application to a rat model of immobilisation osteoporosis, *Med. Biol. Eng. Comput.* **38**(3), 326–332 (2000)
- 24.59 W.A. Merz, R.K. Schenk: Quantitative structural analysis of human cancellous bone, *Acta Anat.* **75**(1), 54–66 (1970)
- 24.60 R. Müller, H. Van Campenhout, B. Van Damme, G. Van Der Perre, J. Dequeker, T. Hildebrand, P. Rüeegsegger: Morphometric analysis of human bone biopsies: A quantitative structural comparison of histological sections and micro-computed tomography, *Bone* **23**(1), 59–66 (1998)
- 24.61 K.K. Nishiyama, G.M. Campbell, R.J. Klinck, S.K. Boyd: Reproducibility of bone micro-architecture measurements in rodents by in vivo micro-computed tomography is maximized with three-dimensional image registration, *Bone* **46**(1), 155–161 (2010)
- 24.62 A. Odgaard: Three-dimensional methods for quantification of cancellous bone architecture, *Bone* **20**(4), 315–328 (1997)
- 24.63 A. Odgaard, H.J. Gundersen: Quantification of connectivity in cancellous bone, with special emphasis on 3-D reconstructions, *Bone* **14**(2), 173–182 (1993)
- 24.64 I.V. Pratt, G. Belev, N. Zhu, L.D. Chapman, D.M. Cooper: In vivo imaging of rat cortical bone porosity by synchrotron phase contrast micro computed tomography, *Phys. Med. Biol.* **60**(1), 211–232 (2015)
- 24.65 P. Rüeegsegger, B. Koller, R. Müller: A microtomographic system for the nondestructive evaluation of bone architecture, *Calcif. Tissue Int.* **58**(1), 24–29 (1996)
- 24.66 P.L. Salmon, A.Y. Sasov: Application of nano-CT and high-resolution micro-CT to study bone quality and ultrastructure, scaffold biomaterials and vascular networks. In: *Advanced Bioimaging Technologies in Assessment of the Quality of Bone and Scaffold Materials*, ed. by L. Qin, H.K. Genant, J.F. Griffith, K.S. Leung (Springer, Berlin 2007)
- 24.67 B. van Rietbergen, H. Weinans, R. Huiskes, A. Odgaard: A new method to determine trabecular bone elastic properties and loading using micromechanical finite-element models, *J. Biomech.* **28**(1), 69–81 (1995)
- 24.68 R.M. Coleman, J.E. Phillips, A. Lin, Z. Schwartz, B.D. Boyan, R.E. Guldberg: Characterization of a small animal growth plate injury model using microcomputed tomography, *Bone* **46**(6), 1555–1563 (2010)
- 24.69 C.L. Duvall, W.R. Taylor, D. Weiss, R.E. Guldberg: Quantitative microcomputed tomography analysis of collateral vessel development after ischemic injury, *Am. J. Physiol. Heart Circ. Physiol.* **287**(1), H302–H310 (2004)
- 24.70 R.E. Guldberg, R.T. Ballock, B.D. Boyan, C.L. Duvall, A.S. Lin, S. Nagaraja, M. Oest, J. Phillips, B.D. Porter, G. Robertson, W.R. Taylor: Analyzing bone, blood vessels, and biomaterials with microcomputed tomography, *IEEE Eng. Med. Biol. Mag.* **22**(5), 77–83 (2003)
- 24.71 A.W. Palmer, R.E. Guldberg, M.E. Levenston: Analysis of cartilage matrix fixed charge density and three-dimensional morphology via contrast-enhanced microcomputed tomography, *Proc. Natl. Acad. Sci. USA* **103**(51), 19255–19260 (2006)
- 24.72 G.L. Kindlmann, D.M. Weinstein, G.M. Jones, C.R. Johnson, M.R. Capecchi, C. Keller: Practical vessel imaging by computed tomography in live transgenic mouse models for human tumors, *Mol. Imaging* **4**(4), 417–424 (2005)
- 24.73 A. Lin, A.W. Palmer, C. Duvall, G. Robertson, M. Oest, B. Rai, M.E. Levenston, R. Guldberg: Contrast enhanced micro-CT imaging of soft tissues. In: *Advanced Bioimaging Technologies in Assessment of the Quality of Bone and Scaffold Materials*, ed. by L. Qin, H.K. Genant, J.F. Griffith, K.S. Leung (Springer, Berlin 2007)
- 24.74 S.R. Stock, G. Wang, B. Müller: Developments in x-ray tomography x, *Proceedings SPIE* (2016), <https://doi.org/10.1117/12.2256419>
- 24.75 ASTM International: *ASTM 1441-11: Standard Guide for Computed Tomography (CT) Imaging* (ASTM International, Subcommittee E07.01 on Radiology (X and Gamma) Method, West Conshohocken 2011)
- 24.76 Wikipedia: SOLEIL, <https://en.wikipedia.org/wiki/SOLEIL> (2016)
- 24.77 S.R. Stock: *MicroComputed Tomography: Methodology and Applications* (Taylor Francis, Boca Raton 2008)
- 24.78 SOLEIL Synchrotron: Synchrotron SOLEIL, <http://www.synchrotron-soleil.fr> (2016)
- 24.79 S.R. Stock: MicroCT systems and their components. In: *Microcomputed Tomography: Method-*

- ology and Applications (Taylor Francis, Boca Raton 2008)
- 24.80 Wikipedia: Charge-coupled device, [https://en.wikipedia.org/wiki/Charge-coupled\\_device](https://en.wikipedia.org/wiki/Charge-coupled_device) (2016)
- 24.81 S.M. Sze, K.K. Ng: *Physics of Semiconductor Devices*, 3rd edn. (Wiley, Hoboken 2006)
- 24.82 B.D. Cullity, S.R. Stock: *Elements of X-ray Diffraction*, 3rd edn. (Prentice-Hall, Upper Saddle River 2001)
- 24.83 J.F. Barrett, N. Keat: Artifacts in CT: Recognition and avoidance, *RadioGraphics* **24**, 1679–1691 (2004)
- 24.84 F.E. Boas, D. Fleischmann: CT artifacts: Causes and reduction techniques, *Imaging Med.* **4**(2), 229–240 (2012)
- 24.85 S.R. Stock: MicroCT in practice. In: *MicroComputed Tomography: Methodology and Applications* (Taylor Francis, Boca Raton 2008)
- 24.86 A.J. Burghardt, G.J. Kazakia, S. Majumdar: A local adaptive threshold strategy for high resolution peripheral quantitative computed tomography of trabecular bone, *Ann. Biomed. Eng.* **35**(10), 1678–1686 (2007)
- 24.87 T.F. Chan, L.A. Vese: Active contours without edges, *IEEE Trans. Image Process.* **10**(2), 266–277 (2001)
- 24.88 J.H. Waarsing, J.S. Day, H. Weinans: An improved segmentation method for in vivo microCT imaging, *J. Bone Miner. Res.* **19**(10), 1640–1650 (2004)
- 24.89 N. Otsu: Threshold selection method from gray-level histograms, *IEEE Trans. Syst. Man Cybern.* **9**(1), 62–66 (1979)
- 24.90 P. Iassonov, T. Gebrenegus, M. Tuller: Segmentation of X-ray computed tomography images of porous materials: A crucial step for characterization and quantitative analysis of pore structures, *Water Resour. Res.* (2009), <https://doi.org/10.1029/2009WR008087>
- 24.91 T. Hara, E. Tanck, J. Homminga, R. Huiskes: The influence of microcomputed tomography threshold variations on the assessment of structural and mechanical trabecular bone properties, *Bone* **31**(1), 107–109 (2002)
- 24.92 I.H. Parkinson, A. Badiei, N.L. Fazzalari: Variation in segmentation of bone from micro-CT imaging: Implications for quantitative morphometric analysis, *Australas. Phys. Eng. Sci. Med.* **31**(2), 160–164 (2008)
- 24.93 S. Tassani, V. Korfiatis, G.K. Matsopoulos: Influence of segmentation on micro-CT images of trabecular bone, *J. Microsc.* **256**(2), 75–81 (2014)
- 24.94 M. Doube: The ellipsoid factor for quantification of rods, plates, and intermediate forms in 3D geometries, *Front. Endocrinol.* **6**, 15 (2015)
- 24.95 P.L. Salmon, C. Ohlsson, S.J. Shefelbine, M. Doube: Structure model index does not measure rods and plates in trabecular bone, *Front. Endocrinol.* **6**, 162 (2015)
- 24.96 A. Larrue, A. Rattner, Z.A. Peter, C. Olivier, N. Laroche, L. Vico, F. Peyrin: Synchrotron radiation micro-CT at the micrometer scale for the analysis of the three-dimensional morphology of microcracks in human trabecular bone, *PLoS One* **6**(7), e21297 (2011)
- 24.97 S. Frolich, H. Leemreize, A. Jakus, X. Xiao, R. Shah, H. Birkedal, J.D. Almer, S.R. Stock: Diffraction tomography and Rietveld refinement of a hydroxypapatite bone phantom, *J. Appl. Crystallogr.* **49**, 103–109 (2016)
- 24.98 J.H. Kinney, N.E. Lane, D.L. Haupt: In vivo, three-dimensional microscopy of trabecular bone, *J. Bone Miner. Res.* **10**(2), 264–270 (1995)
- 24.99 N.E. Lane, J.M. Thompson, G.J. Strewler, J.H. Kinney: Intermittent treatment with human parathyroid hormone (hPTH[1–34]) increased trabecular bone volume but not connectivity in osteopenic rats, *J. Bone Miner. Res.* **10**(10), 1470–1477 (1995)
- 24.100 F. Peyrin, M. Salome, P. Cloetens, A.M. Laval-Jeantet, E. Ritman, P. Rueggsegger: Micro-CT examinations of trabecular bone samples at different resolutions: 14, 7 and 2 micron level, *Technol. Health Care* **6**(5/6), 391–401 (1998)
- 24.101 C. Badea, L.W. Hedlund, G.A. Johnson: Micro-CT with respiratory and cardiac gating, *Med. Phys.* **31**(12), 3324–3329 (2004)
- 24.102 M.L. Bouxsein, S.K. Boyd, B.A. Christiansen, R.E. Guldberg, K.J. Jepsen, R. Müller: Guidelines for assessment of bone microstructure in rodents using micro-computed tomography, *J. Bone Miner. Res.* **25**(7), 1468–1486 (2010)
- 24.103 H. Li, H. Zhang, Z. Tang, G. Hu: Micro-computed tomography for small animal imaging: Technological details, *Prog. Nat. Sci.* **18**, 513–521 (2008)
- 24.104 D.W. Holdsworth, M.M. Thornton: Micro-CT in small animal and specimen imaging, *Trends Biotechnol.* **20**(8), S34–S39 (2002)
- 24.105 S.J. Schambach, S. Bag, L. Schilling, C. Groden, M.A. Brockmann: Application of micro-CT in small animal imaging, *Methods* **50**(1), 2–13 (2010)
- 24.106 K. Umetani, J.T. Pearson, D.O. Schwenke, M. Shirai: Development of synchrotron radiation x-ray intravital microscopy for in vivo imaging of rat heart vascular function. In: *2011 Ann. Int. Conf. IEEE Eng. Med. Biol. Soc* (2011) pp. 7791–7794
- 24.107 K.B. Ghaghada, C.T. Badea, L. Karumbaiah, N. Fetting, R.V. Bellamkonda, G.A. Johnson, A. Annapragada: Evaluation of tumor microenvironment in an animal model using a nanoparticle contrast agent in computed tomography imaging, *Acad. Radiol.* **18**(1), 20–30 (2011)
- 24.108 T. Nakagawa, K. Gonda, T. Kamei, L. Cong, Y. Hamada, N. Kitamura, H. Tada, T. Ishida, T. Aimiya, N. Furusawa, Y. Nakano, N. Ohuchi: X-ray computed tomography imaging of a tumor with high sensitivity using gold nanoparticles conjugated to a cancer-specific antibody via polyethylene glycol chains on their surface, *Sci. Technol. Adv. Mater.* **17**(1), 387–397 (2016)
- 24.109 S. Stock: *X-ray Computed Tomography. Characterization of Materials*, 2nd edn. (Wiley, New York 2012)

- 24.110 D. Paganin, S.C. Mayo, T.E. Gureyev, P.R. Miller, S.W. Wilkins: Simultaneous phase and amplitude extraction from a single defocused image of a homogeneous object, *J. Microsc.* **206**, 33–40 (2002)
- 24.111 C.P. Richter, W. Liddy, A. Vo, H. Young, S. Stock, X.H. Xiao, D. Whitton: Evaluation of neural cochlear structures after noise trauma using X-ray tomography, *Proceedings SPIE* (2014), <https://doi.org/10.1117/12.2062385>
- 24.112 P.V. Granton, S.I. Pollmann, N.L. Ford, M. Drangova, D.W. Holdsworth: Implementation of dual- and triple-energy cone-beam micro-CT for postreconstruction material decomposition, *Med. Phys.* **35**(11), 5030–5042 (2008)
- 24.113 C.L. Lee, H. Min, N. Befera, D. Clark, Y. Qi, S. Das, G.A. Johnson, C.T. Badea, D.G. Kirsch: Assessing cardiac injury in mice with dual energy-microCT, 4D-microCT, and microSPECT imaging after partial heart irradiation, *Int. J. Radiat. Oncol. Biol. Phys.* **88**(3), 686–693 (2014)
- 24.114 N. Manohar, F.J. Reynoso, P. Diagaradjane, S. Krishnan, S.H. Cho: Quantitative imaging of gold nanoparticle distribution in a tumor-bearing mouse using benchtop x-ray fluorescence computed tomography, *Sci. Rep.* **6**, 22079 (2016)
- 24.115 X. Chen, H. Zhu, X. Huang, P. Wang, F. Zhang, W. Li, G. Chen, B. Chen: Novel iodinated gold nanoclusters for precise diagnosis of thyroid cancer, *Nanoscale* **9**(6), 2219–2231 (2017)
- 24.116 M.E. Birkbak, H. Leemreize, S. Frolich, S.R. Stock, H. Birkedal: Diffraction scattering computed tomography: a window into the structures of complex nanomaterials, *Nanoscale* **7**(44), 18402–18410 (2015)
- 24.117 S.R. Stock, J.D. Almer: Diffraction microcomputed tomography of an Al-matrix SiC-monofilament composite, *J. Appl. Crystallogr.* **45**, 1077–1083 (2012)
- 24.118 T.M. Breunig, S. Stock, S.D. Antolovich, J.H. Kinney, W.N. Massey, M.C. Nichols: A framework relating macroscopic measures and physical processes of crack closure of Al-Li Alloy 2090. In: *Proc. Fract. Mech. Twenty-Second Symp.* (1992)
- 24.119 A. Guvenilir, T.M. Breunig, J.H. Kinney, S.R. Stock: Direct observation of crack opening as a function of applied load in the interior of a notched tensile sample of Al-Li 2090, *Acta Mater.* **45**(5), 1977–1987 (1997)
- 24.120 J.H. Kinney, T.M. Breunig, T.L. Starr, D. Haupt, M.C. Nichols, S.R. Stock, M.D. Butts, R.A. Saroyan: X-ray tomographic study of chemical vapor infiltration processing of ceramic composites, *Science* **260**(5109), 789–792 (1993)
- 24.121 S.B. Lee, S.R. Stock, M.D. Butts, T.L. Starr, T.M. Breunig, J.H. Kinney: Pore geometry in woven fiber structures: 0 degrees/90 degrees plain-weave cloth layup preform, *J. Mater. Res.* **13**(5), 1209–1217 (1998)

### Angela S.P. Lin



Phil and Penny Knight Campus for  
Accelerating Scientific Impact  
University of Oregon  
Eugene, OR, USA  
[al81@uoregon.edu](mailto:al81@uoregon.edu)

Angela Lin achieved her Masters degree in mechanical engineering from the Georgia Institute of Technology in 2002. She has worked as a Research Engineer in Dr. Robert Guldberg's Musculoskeletal Research Laboratory (Georgia Institute of Technology 2003–2008, University of Oregon 2018–present), focusing on studying and treating orthopedic tissue degeneration and disease, utilizing such tools as microCT imaging and mechanical testing to perform structural and functional characterization.

### Stuart R. Stock

Northwestern University  
Chicago, IL, USA  
[s-stock@northwestern.edu](mailto:s-stock@northwestern.edu)



Stuart R. Stock received his PhD from the University of Illinois at Champaign-Urbana in 1983 and was on the faculty of Georgia Institute of Technology for 16 years before joining Northwestern University in 2001. In 1986, he published the first of his more than 130 papers on x-ray micro-computed tomography.

### Robert E. Guldberg

Phil and Penny Knight Campus for  
Accelerating Scientific Impact  
University of Oregon  
Eugene, OR, USA  
[guldberg@uoregon.edu](mailto:guldberg@uoregon.edu)



Robert Guldberg received his PhD from the University of Michigan in 1995. He directed the Petit Institute for Bioengineering and Bioscience at the Georgia Institute of Technology 2009–2018. In 2018, he became the Inaugural Executive Director of the Knight Campus at the University of Oregon. His research is focused on musculoskeletal regenerative medicine, mechanobiology, and orthopedic implants.